Summer 2012

Doppler Wind Lidar Observations of a Wildland Fire Plume

Allison Marie Charland
San Jose State University

DOPPLER WIND LIDAR OBSERVATIONS OF A WILDLAND FIRE PLUME

A Thesis

Presented to

The Faculty of the Department of Meteorology and Climate Science

San Jose State University

In Partial Fulfillment

of the Requirements for the Degree

Master of Science

by

Allison M. Charland

August 2012

The Designated Thesis Committee Approves the Thesis Titled

DOPPLER WIND LIDAR OBSERVATIONS OF A WILDLAND FIRE PLUME

by

Allison M. Charland

APPROVED FOR THE DEPARTMENT OF METEOROLOGY
AND CLIMATE SCIENCE

SAN JOSÉ STATE UNIVERSITY

August 2012

Dr. Craig B. Clements	Department of Meteorology and Climate Science
Dr. Sen Chiao	Department of Meteorology and Climate Science
Dr. Andrew Oliphant	Department of Geography, San Francisco State University

ABSTRACT

DOPPLER WIND LIDAR OBSERVATIONS OF A WILDLAND FIRE PLUME

by Allison M. Charland

Observations in the vicinity of a wildland fire showed the development of a convergence zone downwind of the convection column. These observations were obtained during a prescribed burn in complex terrain east of San Jose, California. A ground-based Halo Photonics, Ltd. Stream Line 75 Lidar acquired Doppler wind velocities and backscatter intensity in and around the fire plume from multiple vertically pointing, PPI, and RHI scans while a ASC miniSodar obtained vertical wind and turbulence profiles downwind. These observations allowed for the study of the kinematic structure and spatial and temporal evolution of the fire plume. Observations showed velocities accelerating at the plume boundary, indicating an inflow into the base of the convective updraft. The development of a convergence zone was observed by decreases in radial velocity of 3-5 m s^{-1} downwind of the plume compared to velocities near the fire front. This deceleration of the wind was also observed from sodar measurements downwind of the fire. An increase in potential temperature within the plume of 3.0-4.4 K was observed with an increase in mixing ratio of 0.5-1.0 g kg^{-1}. Increased turbulent mixing was found within the plume with an increase in turbulent kinetic energy of 3 m^2 s^{-2} within the plume and updraft velocities near 1 m s^{-1}. In addition, methods were developed for estimating the fire spread rate and the rate of spread of the plume.

ACKNOWLEDGEMENTS

I would like to express gratitude to my thesis committee for their help and guidance in writing this thesis. I would like to thank my advisor, Dr. Craig Clements, for all the support with my research as well as the motivation to keep working hard. I would also like to thank the other members of my committee, Dr. Sen Chiao and Dr. Andrew Oliphant, for their comments and suggestions for improving my thesis.

I would like to acknowledge Daisuke Seto for all his help in the field and for his assistance with instrumentation and programming. Also, a special thanks to Dianne Hall and Richard Bagley for their help with field work and assistance with the experiment set up.

I would like to acknowledge Battalion Chief Dave McLean and Calfire for their help in managing the prescribed burn. This work has been supported by research grants from NSF (#0960300) and the USDA (USDA #07-JV-11242300-073).

TABLE OF CONTENTS

LIST OF FIGURES……...……vii

LIST OF TABLES……..….x

1. Introduction……1

2. Lidar Background……..6

3. Methodology and Experimental Design……8

    a. Instrumentation……..10

    b. Experimental Lidar Scanning Strategies……...…….……14

    c. Lidar Data Processing……15

4. Results……..18

    a. Preliminary Studies……19

        1) Urban Aerosol Layer Observations…….19

        2) Along-valley Winds…….24

    b. Thermodynamic Plume Properties…….……32

    c. Fire-induced Circulations……...34

    d. Plume Turbulence……..43

    e. Convection Core Tracking…….46

5. Conclusions……..47

REFERENCES……..50

LIST OF FIGURES

1. Map of Joseph D. Grant County Park showing the burn unit outlined in black and including the instrument placement……..…...10
2. Temperature (red) and dewpoint temperature (blue) profiles from radiosonde soundings at 0901 PST (solid) and 1149PST (dashed) on 13 July 2011…….12
3. Wind rose plots of wind speed and direction for 4 RAWS locations from 800-1800 PST on 13 July 2011. Map showing the location of each station is shown with the black box indicating the experiment area……13
4. Wind speed and direction profiles from radiosonde launched from the ridgetop at 1644 PST……..14
5. Backscatter intensity (SNR+1) as a function of the range gate (a) is shown. The function *D(r)* is shown for the front (blue) and *F(r)* is shown for the (b) end (green) boundaries……...……....17
6. Vertical velocity (m s^{-1}) profiles over time from lidar located on the top of a building in downtown San José on 24 September 2011.…….……..……..21
7. Vertical velocity (m s^{-1}) profiles over time from lidar located on the top of a building in downtown San José on 25 September 2011……...…….…..22
8. Vertical velocity (m s^{-1}) profiles over time from lidar located in downtown San José on 3 November 2011……23
9. RHI lidar scans of the valley along a 150^{o} azimuth angle and elevation angles varying from 0^{o} to 85^{o} by increments of 5^{o} on 9 April 2011……...25

10. RHI lidar scans along the valley atmosphere along a 145^{o} azimuth angle and elevation angles varying from 0^{o} to 80^{o} by increments of 5^{o} on 9-10 April 2011…...26
11. Vertical velocity (m s^{-1}) profiles over time from lidar located at valley floor on 9 April 2011……27
12. Radiosonde sounding launched from the valley floor at 1600 PST on 9 April 2011 with profiles of wind speed and direction and potential temperature and mixing ratio.……..……28
13. Radiosonde sounding launched from the valley floor at 2000 PST on 9 April 2011 with profiles of wind speed and direction and potential temperature and mixing ratio.……..……28
14. Radiosonde sounding launched from the valley floor at 0600 PST on 10 April 2011 with profiles of wind speed and direction and potential temperature and mixing ratio……..……..……30
15. RHI lidar scans along the valley along a 145^{o} azimuth angle and elevation angles varying from 0^{o} to 80^{o} by increments of 5^{o} on 10 April 2011…….30
16. Vertical velocity (m s^{-1}) profiles over time from lidar located at valley floor on 10 April 2011……31
17. Water vapor mixing ratio and potential temperature profiles from radiosonde launched from the ridgetop location at 1237 PST and 1644 PST and profiles from the radiometer at the same times on 13 July 2011……...…33

18. PPI lidar scans through the plume at specified times with the lidar located at the origin (0,0). The images display the radial velocity component (m s^{-1}). The black contours outline the areas of high backscatter intensity indicating the location of the plume……..……...…….36

19. Doppler radial velocity at 1750 PST on 13 July 2011 for a 10 ^{o} elevation angle and an azimuth angle of 68^{o} at 1757 PST of 62^{o} at 1800 PST of 65^{o} and at1801 PST of 64^{o}. The location of the convergence zone is indicated by the red dashed line…..…..37

20. 10 min averaged wind speeds measured at 20 m AGL from the sodar. Red dashed line indicates the time the fire was ignited…….…..40

21. RHI lidar scans through the plume along a 95^{o} azimuth angle at specified times with the lidar located at the origin (0,0). The black contours indicate areas of high backscatter intensity displaying the location of the plume…….…….41

22. Time-height contours of vertical velocity and turbulence kinetic energy measured from the sodar on 13 July 2011 from the ridge top location……45

23. PPI lidar scans through the plume at specified times. The top images with the white stars show the location of the most intense part of the plume or the convection core. The bottom images show the regions of high backscatter intensity overlaid with the boundaries of the plume…….……...……47

LIST OF TABLES

1. Site identifications, locations, and instrumentation for burn experiment on 13 July 2011.....9

1. Introduction

While wildland fires are a natural occurrence and help in the functioning of ecosystems, they can destroy communities around the globe, resulting in high economic costs (Westerling et al. 2006; Bowman et al. 2009). A key aspect in battling these wildfires is understanding the physical mechanisms occurring within a fire that determine the fire growth and behavior. While advances in understanding wildfire dynamics have been made with the development of coupled fire-atmospheric modeling systems (Coen et al. 2004; Mell et al. 2007; Linn et al. 2007; Mandel et al. 2009), there is a lack of observational data for validating these modeling systems. Therefore, high spatial and temporal observations in the vicinity of a wildland fire plume are required to better understand the dynamics of fire-atmosphere interactions and to provide a dataset for coupled fire-atmosphere model validation. Because of the difficulty in using in situ instrumentation in the wildland fire environment, remote-sensing instrumentation becomes most practical for both personnel safety and instrument protection since it allows the region around wildland fires to be probed from a safe distance.

Wildland fires are mainly wind driven. The key meteorological conditions leading to the intensification of wildland fires are high wind speeds, high air temperatures, and low humidities. A plume is generated by the buoyancy forces that arise from the large amount of heating at the surface from the fire front or combustion zone. The behavior of the plume is dependent on the winds in the lower 2-3 km of the atmosphere (Banta et al. 1992). Strong updrafts can be generated within the plume when winds are fairly light due to the buoyancy from the hot gases in the convection column.

In accordance with the conservation of mass, the strong updraft in the plume will subsequently result in downward air motion in other areas that can lead to a strong outflow at the surface affecting fire spread (Banta et al. 1992; Potter 2011). Another recognized dynamic feature of a wildfire plume is the rear inflow, which descends on the upwind side of the fire. The path of the rear inflow is hard to observe; therefore, there is not much known about its characteristics (Clements et al. 2007; Potter 2011). Understanding the structure within the plume then becomes important in the study of fire behavior.

Several observational campaigns have studied the conditions near or within wildland fires to gain a better understanding of fire behavior and fire-atmosphere interactions. Previous studies have used in situ measurements to look at temperature structure, heat, water, and CO_2 fluxes within the regions of a burn (Clements 2006). In the lower 40 m of a plume, there was an observed increase in temperature of up to 20 ^{o}C and an increase in water vapor mixing ratio of 2 g kg^{-1}. The FireFlux experiment has been the most comprehensive study looking at fire-induced winds from a grass fire. During this experiment, large updrafts of ~10 m s^{-1} were found around the fire (Clements et al. 2007). Downward vertical motion was observed behind the fire line with velocities at half the magnitude of the updrafts. Downwind of the burn perimeter, strong turbulent downdrafts were also observed. Also observed was the production of turbulence during the fire due to the increased variance of the observed wind at the fire front. Observations showed turbulent kinetic energy increasing during the fire front passage from 2 m^2 s^{-2} to nearly four or five times greater than the ambient turbulence. It was found that wind

shear that develops from a rapid increase in velocity at the surface near the fire front contributes to enhanced turbulence. Behind the fire line, there is a decrease in turbulence with subsidence (Clements et al. 2008). The thermodynamic structure of the plume was also previously studied using in situ temperature measurements. Rapid heating and cooling within the plume were found, indicating a fast rate of spread of the fire (Clements 2010).

Due to the difficulty in placing instruments near wildland fires, some studies have used various types of imagery to study fire-induced winds. Coen et al. (2004) used infrared imagery to examine the dynamics of a crown fire. The wind field could be derived from an infrared image plane using an image-flow-analysis technique. Using this technique, the horizontal wind speeds were observed, showing a strong inflow into the base of the convective updrafts in the plume. The average spread rate of 0.75-1.11 m s^{-1} was also observed. Video photography was used by Dold and Zinoviev (2009) to observe the changes in a light colored piece of cloth that was tied to vegetation downwind to interpret the winds near the fire. Observations showed that the cloth was influenced by the winds from the fire as it progressed towards the vegetation. However, it was observed that the cloth was undisturbed by the wind flow during certain times throughout the burn indicating a decrease in wind and the development of a convergence zone downwind of the fire.

In a modeling study by Clark et al. (1996), fire line dynamics were examined using a coupled atmosphere-fire model. The results showed the development of a

convergence zone produced by hot convective columns ahead of a propagating fire. With higher ambient wind speeds, the convective column tilts downstream and can shift the center of the low-level convergence pattern. The convergence pattern is responsible for the parabolic shape of the fire line as it draws in low-level air equally from all sides.

Remote sensing instrumentation allow for obtaining observations over large areas with better temporal and spatial resolution than would be possible with balloon soundings and surface observations alone. Few studies have been conducted near wildland fires using remote-sensing measurements of smoke plumes. However, Banta et al. (1992) used a Doppler lidar and Doppler radar to obtain smoke-column observations of two forest fires. Of the two fires, one was a wildfire, while the other was a prescribed burn. During the first fire, a pair of counterrotating horizontal vorticies occurred within the smoke-column, using the Doppler radar. The velocity structure of a horizontal plane through a smoke plume mapped from the Doppler radar showed faster flow along the edges of the plume with decreased flow along the centerline. The second fire was observed with the lidar, indicating flow convergence and anticyclonic whole-column rotation. Estimated peak vertical velocities of 15 m s^{-1} were found along with vorticity of approximately 10^{-2} s^{-1}. An industrial fire was observed by three radars showing the spread in the fire plume as it was advected downwind (Rogers and Brown 1997). Lidar measurements and an artificial smoke tracer over flat terrain were used by Jorgensen et al. (1992) to calculate plume statistics. This experiment enabled the study of the variability and fluctuations in dispersing aerosol plumes in the atmospheric surface layer. Sofiev et al. (2012) evaluated a new method for determining smoke-injection heights of

wildland fires using observations from the Multi-angle Imaging SpectroRadiometer (MISR) instrument on the NASA Terra satellite.

Lidar instrumentation has been used for many different applications. Various studies have examined wind flow regimes in complex terrain using a lidar. Rucker et al. (2007) studied the along-valley structure of daytime thermally driven flows in the Wipp Valley in Austria. The study involved using partial conical scans to determine flow along the valley. Interactions between complex terrain and the boundary layer were studied using a lidar by Barkwith and Collier (2011). In this study, a laminar flow PPI model was used to distinguish turbulence structures in the region. Other studies have used methods to estimate mean wind and the parameters of small-scale turbulence of lidar data (Frehlich 1996; Frehlich and Cornman 2001; Smalikho 2002; Banakh and Werner 2005; Frehlich 2008). During the Terrain-induced Rotor Experiment (T-REX) in April-May 2006, turbulence parameters were estimated by processing radial velocity structure functions from retrieved lidar data (Krishnamurthy et al. 2011). Lidar observations of the boundary layer in a tropical rainforest by Pearson et al. (2010) examined the dispersion and transport processes within the forest canopy.

In this study, observations of the kinematic structure of a wildland fire plume using remote-sensing instrumentation are analyzed. On 13 July 2011, a prescribed burn was conducted in complex terrain east of San José, California. A Doppler wind lidar system acquired measurements through the plume for the duration of the burn while a sodar obtained wind and turbulence profiles downwind of the plume. Section 2 details

the background and characteristics of the lidar system. Section 3 describes the experimental design and methods applied to this experiment, including preliminary studies conducted to design a suite of lidar scanning strategies. Results and discussion from the analyses of the lidar and sodar observations are discussed in Section 4. Section 5 contains conclusions drawn from the key findings of this experiment.

2. Lidar Background

This study examines the radial velocity and the backscatter intensity from a Halo Photonics, Ltd. Stream Line 75 Doppler wind lidar. Pearson et al. (2009) provides a detailed description of characteristics and performance of the lidar. This lidar emits an eye-safe infrared light at a wavelength of 1.5 μm, which is scattered by aerosols in the atmosphere. The lidar transmits laser pulses into the atmosphere at a rate of 10 Hz. The fraction of energy of the return signal received by the lidar is a function of aerosol density. The shift in the frequency of the returned signal is due to the movement of aerosols in the atmosphere by the wind. The frequency is a function of the radial component of the wind speed with respect to the location of the lidar. Also, the time that it takes for the signal to be returned is a function of distance from the lidar. The lidar is equipped with a 75 mm aperture all-sky optical scanner enabling the scan of the lidar from 0-360^{o} azimuth angles and -15-195^{o} elevation angles. There are up to 550 possible user-defined range gates at 24 m spacing with the minimum range at 80 m and maximum range at 9.6 km. For this experiment, the maximum range was 3500 m since the location of the firing operations were within 1 km of the lidar. The temporal resolution varied from 0.1-180 s depending on the type of scan scheduled. While scanning a region, the

stationarity assumption must be applied. This assumes that the atmosphere does not statistically change over the time it takes to complete a scan (Stull 1988).

Different lidar scanning techniques can be applied to study the velocity field of the atmosphere and the structure of a smoke plume. The first technique is a stare, which allows for observing the change in the boundary layer height and vertical velocity at one location over time (Lothon et al. 2009). In this technique, the lidar emits a vertically pointed beam and returns the Doppler radial velocity, which represents the profile of the vertical velocity with height. A Doppler Beam Swinging (DBS) scan obtains wind speed and direction profiles using a 3-beam profiling method. This method uses a vertically pointed beam, a beam tilted east, and a beam tilted north to calculate wind speed and direction up to 9600 m in increments of 24 m. For this study, a suite of scan schedules were developed in order to have the ability to scan in any direction. A Range Height Indicator (RHI) scan uses a fixed azimuth angle while varying the elevation angle in order to obtain a vertical cross section through the atmosphere. Plan Position Indicator (PPI) scans were also performed, using a fixed elevation angle while varying azimuth angles to get a nearly horizontal cross section of the atmosphere.

Different methods were used for post-processing the lidar data to correct for instrumental errors. Since the minimum range for the lidar is 80 m, the first step in processing the data was to remove any data within the first 100 m to eliminate any corrupted data. The raw data examined from the lidar also contain fluctuating velocity values after a certain point as the signal is attenuated. The point at which the data

becomes irregular is different for each scan. Therefore, an algorithm was created to determine the location where the difference between two adjacent values of velocity exceeds an unrealistic value. For these cases, the threshold value for this difference was set to ±7 m s^{-1} with the assumption that a velocity change of this magnitude between 30 m is unrealistic. Since the velocity data beyond this point were considered unrealistic, it was assumed that any backscatter intensity data retrieved was also invalid and should not be used in analyses. Therefore, all backscatter data beyond that point were also removed.

3. Methodology and Experimental Design

Prescribed fire is widely used in California in order to manage vegetation and reduce the risk of larger wildfires. The prescribed burn conducted in this experiment provided a great opportunity to examine the velocity field around a wildland fire and plume to study fire-induced circulations. In order to study the winds influenced by a wildland fire, various instruments were deployed in and around the prescribed burn unit. The instrumentation for this experiment, detailed in Table 1, included the scanning Doppler wind lidar, a sodar, a micrometeorological tower, and two Remote Automated Weather Stations (RAWS). The map of the burn unit and instrument placement for this experiment is shown in Fig. 1. The burn unit area, outlined in black, included approximately 660 acres of oak woodland in complex terrain ranging in elevation from 450 to 800 m ASL. The fire was ignited from the northeast corner of the burn unit at the top of the ridge, allowing for the fire to spread slowly downslope. Fire crews continued dropping fire along different lines throughout the day to keep the fire burning down the slope.

Table 1. Site identifications (ID), locations, and instrumentation for experiment 13 July 2011. Here, WS is wind speed, WD is wind direction, T is Temperature, RH is relative humidity, and P is pressure.

ID	Lat/Lon (o, min, sec)	Elevation (m MSL)	Instrument type/model
SODAR	37°20'41.88"N 121°41'06.78"W	823	ASC-4000 miniSODAR
LiDAR	37°20'26.58"N 121°43'10.86"W	492	Halo Photonics, Ltd. Stream Line 75
Ridge RAWS	37°20'01.28"N 121°42'50.29"W	836	WS/WD: RM Young 5103, T/RH: Campbell Sci., Inc., CS-215
Valley RAWS	37°20'26.37"N 121°43'10.76"W	491	WS/WD: RM Young 5103, T/RH: Campbell Sci., Inc., CS-215, P: Campbell Sci., Inc., CS-106
In situ Tower	37°20'28.32"N 121°41'03.24"W	783	T/RH: Campbell Sci., Inc., CS-215 WS/WD: RM Young 81000 Sonic Anemometer

On the morning of the burn on 13 July 2011, an upper-level trough contributed to cloudy conditions with slight drizzle that kept the temperatures cool, humidity high, and fuels wet. At the site, a moist layer extended from the surface to 500 m AGL, as indicated in the radiosonde sounding launched from the valley location at 0900 PST (Fig. 2). Around 1100 PST, the clouds began to dissipate, and the lower boundary layer dried out by 1149 PST (Fig. 2). For the duration of the experiment, the prevailing surface winds were from the west-northwest (Fig. 3a-b) with more westerly winds along the ridge. Winds observed from other RAWS around the region were more southerly (Fig. 3c-d). The sounding from 1644 PST showed northwesterly winds near the surface with southwesterly winds aloft (Fig. 4). Moisture in the morning, in combination with light wind speeds, led to low potential for an intense fire. Total heat flux of ~4 kW m^{-2}, measured from the tower during the time of the fire front passage (not shown), indicated a low intensity fire, typical for a prescribed burn.

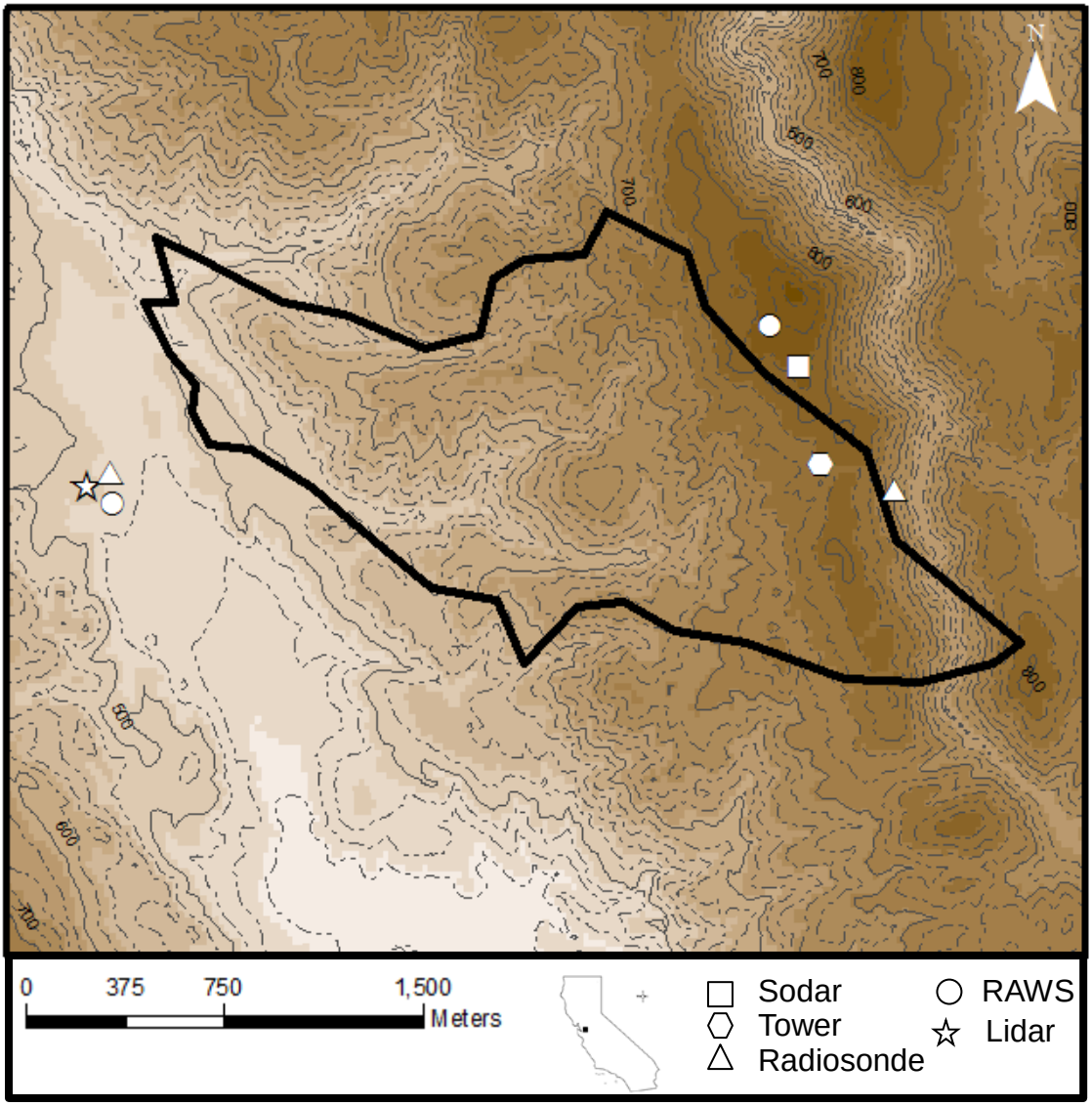

Fig. 1. Map of Joseph D. Grant County Park showing the burn unit outlined in black and including the instrument placement. Darker shading represents higher terrain.

a. Instrumentation

The remote-sensing instrumentation deployed for this experiment included the Doppler wind lidar for winds and aerosol backscatter, a Radiometrics, Inc., MP-3000A profiling radiometer for temperature and humidity profiles, and the ASC-4000

miniSoDAR to capture the vertical wind and turbulence structure. In addition, surface conditions were measured using a micrometeorology tower for high frequency turbulence measurements within the burn unit, and two RAWS for ambient surface conditions. Two radiosonde systems, a GRAW GS-E and a Vaisala, Inc., DigiCora MW31, obtained temperature and wind profiles. Radiosondes were released from both the upwind valley location as well as downwind and into the plume from the ridgetop location.

In order to measure ambient surface conditions in the area, one RAWS station was placed upwind of the burn area at a lower elevation and another was placed on the ridgetop. Each station had a CS215 temperature and relative humidity sensor, and an RM Young 5103 prop anemometer. Temperature, relative humidity, and wind speeds were averaged over 1-minute intervals, and wind-direction was measured at every minute.

A 6.7-m micrometeorology tower was deployed on the ridgetop within the burn unit to obtain high-frequency measurements during the fire front passage. A 3D sonic anemometer sampled temperature and u, v, and w winds at 10 Hz at 6 m AGL. Total and radiative heat fluxes emitted as the fire front passed the tower were measured from a Schmidt-Boelter heat flux sensor.

The sodar was deployed on the ridge downwind of the burn unit to obtain measurements near the plume and ignition line to validate lidar data. Sound detection and ranging (sodar) remote sensing instruments are acoustic profilers that measure wind speed, direction, and turbulence characteristic in the lower boundary layer. Wind speed and direction, in addition to turbulence statistics, were averaged every ten minutes from 20-200 m in increments of 5 m.

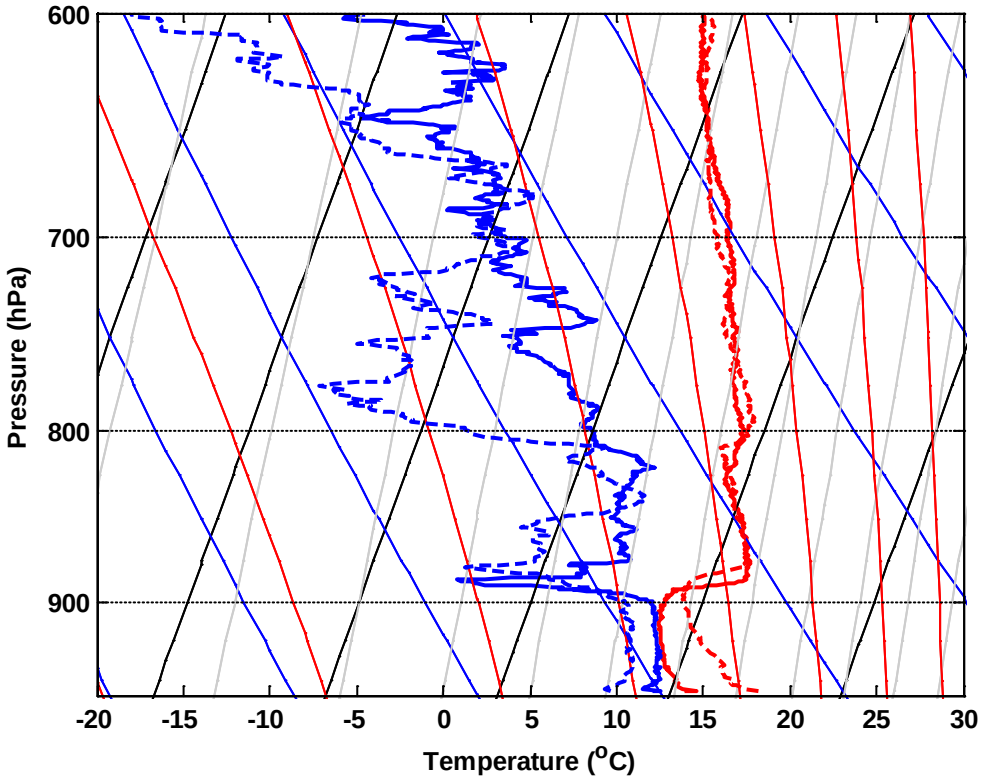

Fig. 2. Temperature (red) and dewpoint temperature (blue) profiles from radiosonde soundings at 0901 PST (solid) and 1149 PST (dashed) on 13 July 2011.

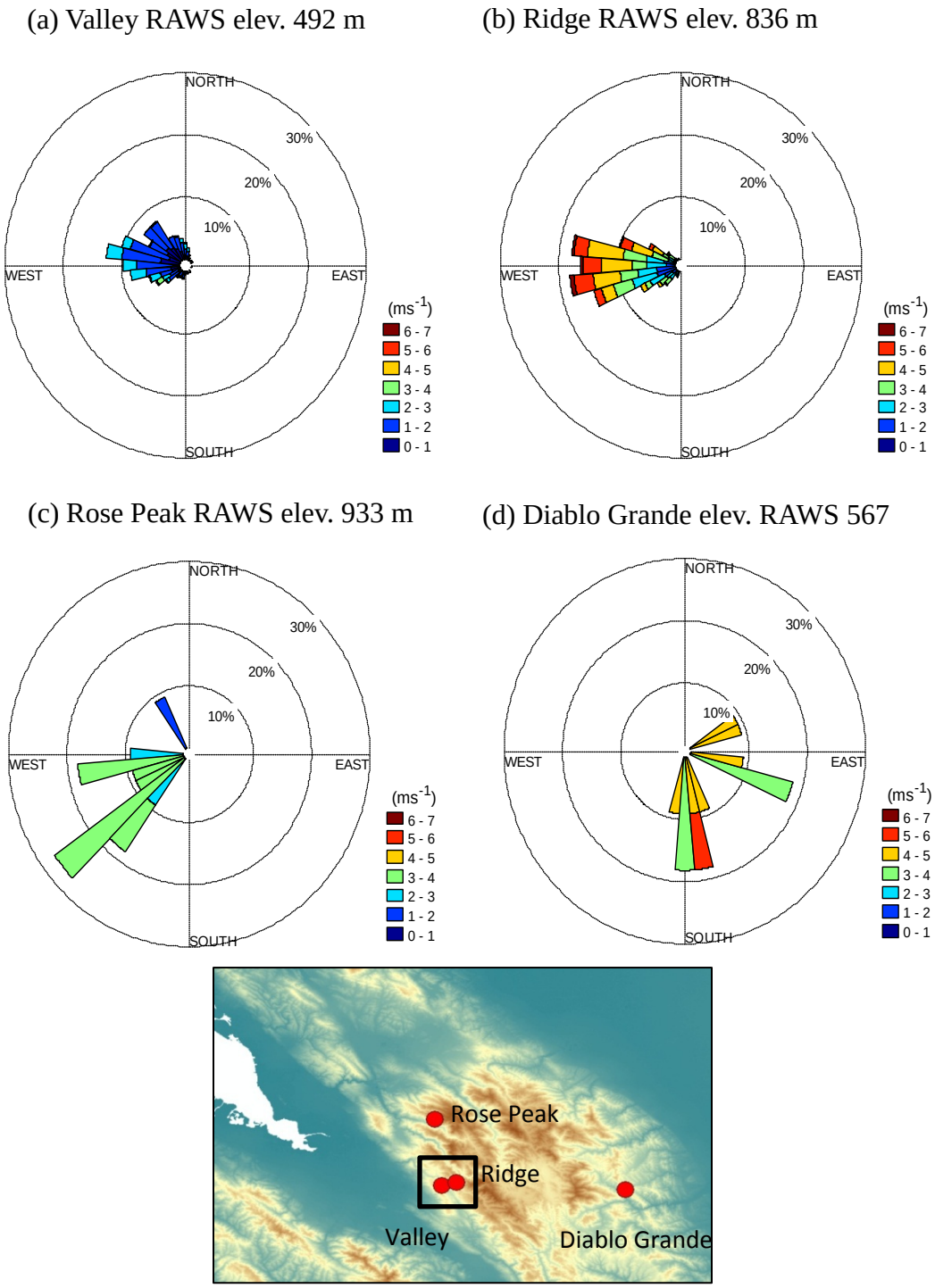

Fig. 3. Wind rose plots of wind speed and direction at 4 RAWS locations (a-d) from 800-1800 PST on 13 July 2011. Map showing the location of each station is shown with the black box indicating the experiment area.

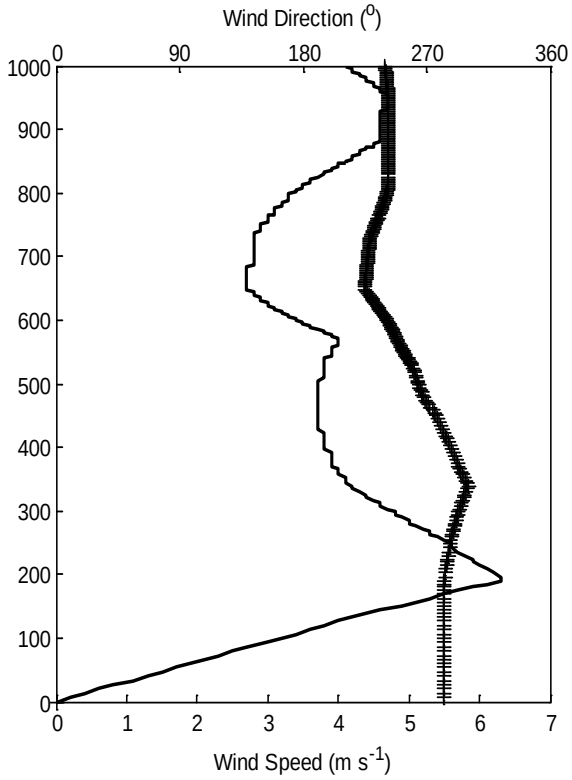

Fig 4. Wind speed and direction profiles from radiosonde launched from the ridgetop at 1644 PST.

b. Experimental Lidar Scanning Strategies

Depending on the location of the fire, various lidar scanning angles were tested to obtain the best observations in and around the plume. The elevation angle was adjusted for scans to avoid scanning surrounding terrain and to optimize the area of the plume scanned. In this study, an azimuth angle of 95^{o} and elevation angles ranging between 7.5-45^{o} in increments of 2.5^{o} were used for the RHI scans. An elevation angle of 10^{o} and azimuth angles ranging from 30-70^{o} in increments of 1.0^{o} were also used for the PPI scans.

c. Lidar Data Processing

Lidar observations were used to examine the kinematic structure in the vicinity of a wildland fire. In order to study the winds near the fire, the near-edge smoke boundaries of a plume can be determined using the backscatter intensity from the lidar scans. Previous studies have developed algorithms that can determine the boundaries of a plume by looking at the gradient of backscatter signals over different distances or range gates. Since the backscatter intensity can vary greatly in each scan, it is difficult to determine the region of the smoke boundary by using a specific threshold value. Kovalev et al. (2005) determined a method for determining the near-edge smoke boundaries from PPI lidar scans. The method determines the boundary by the location of the maximum gradient of the ratio of the backscatter intensity to the integral of the backscatter intensity from the first range gate to the current range gate. The boundary was calculated for each azimuth angle and at each range gate using:

$$D(r) = \frac{d}{dr}\left[\frac{B(r)}{\int_{r_{min}}^{r} B(r)dr}\right] \quad (1)$$

where, $B(r)$ is the backscatter intensity at range gate, r, and r_{min} is the starting range gate. The location of the maximum of $D(r)$ for each azimuth angle indicates the location of the plume boundary closest to the lidar for each scan. This method worked well for finding the zones of multi-layered smoke plumes. However, sometimes the maximum would be at a location that was not necessarily the edge boundary but at a point within the plume.

In these cases, further processing was required for locating the boundary. Similar techniques have also been used for determining cloud height and layers from lidar data (Pal et al. 1992; Chen et al. 2010).

Following Kovalev et al. (2005), the plume boundaries in this experiment can be found by using Eq. 1. This algorithm worked well for the determination of the boundary of an aerosol plume because it eliminated the need for using a criteria value to recognize the difference between the plume and clear air, which can be dramatically different depending on the intensity of the fire. The end boundary, or downwind edge of the plume, can also be determined using a slight modification to Eq. (1). Instead of taking the integral from the first range gate, a reverse integral can start from the last range gate and integrate forward to find the boundary at the outer edge of the plume. The accuracy of the end boundary depends on the validity of the lidar data behind the plume. In studies where cloud top height was determined from lidar data alone, it was difficult to distinguish between the backscatter signal decreasing due to total attenuation within the cloud and where the top of the cloud is reached. Venema et al. (2000) compared lidar and radar measurements of cloud top height to determine if the height found was significantly different. The cases where the height differed by ~100 m were determined to be due to total attenuation of the signal. In this study, the validity of the backscatter data within and beyond the plume is determined by the examination of the Doppler radial velocity returned.

As discussed in Section 2, at a certain range gate the velocity fluctuates due to attenuation of the signal. All the data beyond the range gate at which the fluctuation

begins to occur are then considered invalid and removed. Therefore, from the analysis of all scans, the boundaries determined by the algorithm were within the region of valid data. In Fig. 5a, the backscatter signal is shown with the peak indicating the location of the smoke plume. The front and outer edge of the plume boundaries, shown in Fig. 5b, indicate that the algorithm was successful in finding the location both in front and behind the plume.

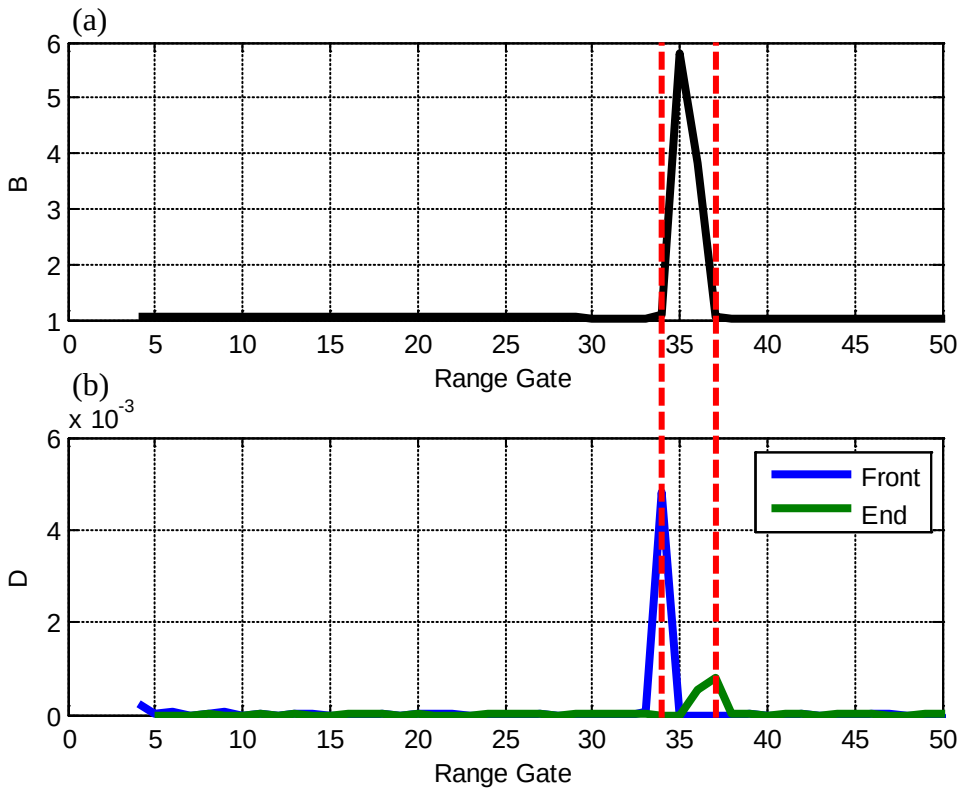

Fig. 5. Backscatter intensity (SNR+1) as a function of the range gate (a) is shown. The peak in backscatter intensity at range gate 35 corresponds to the region of the plume. The function *D(r)* is shown for the front (blue) and end (green) boundaries (b).

When the lidar beam hits surrounding terrain the backscatter intensity increases dramatically. If this occurs during a scan then the algorithm will not be able to determine

the difference between terrain and the plume boundary. Thus, finding the elevation angle that will avoid the terrain is important for determining the plume boundary.

Determining the plume height is important for forecasting plume transport and smoke dispersion in air quality applications. The use of a scanning Doppler lidar can provide higher temporal and spatial resolution measurements of plume height during active wildland fire events than satellite estimates. An algorithm similar to Eq. (1) was used to determine plume height for the RHI scans. Instead of integrating the backscatter intensity across all range gates for a specified azimuth angle, the integral is taken across the elevation angles at a specified range gate. By integrating from a higher to lower elevation angle, the height the plume is identified as the location where the maximum gradient of the backscatter intensity occurs.

4. Results

In order to begin testing the lidar system, the lidar was placed on the roof of Duncan Hall at San José State University (SJSU), which is located in downtown San José, CA. By running the lidar continuously in the stare mode, the urban aerosol layer could be observed over time. While the beam is pointing at a 90^{o} elevation angle, the velocity retrieved corresponds to the vertical velocity in the aerosol layer. Since the lidar determines the velocity by the Doppler shift of the return signal off of the aerosols within the boundary layer, the height of the aerosol layer can be determined as the location where the lidar loses the signal. A second pilot study was conducted in April 2011 to study along-valley winds in a narrow mountain valley east of San José.

a. Preliminary Studies

1) Urban Aerosol Layer Observations

Previous studies have examined the characteristics of the urban boundary layer using a scanning Doppler lidar. Menut et al. (1999) studied the boundary layer evolution in Paris during winter atmospheric pollution events. Menut et al. used a method to determine the boundary layer height on a large set of lidar data under different meteorological conditions. The Basel UrBan Boundary Layer Experiment (BUBBLE), conducted in Basel, Switzerland, studied the urban boundary layer structure (Rotach et al. 2005). This experiment included a lidar near the city center, which obtained atmospheric aerosol vertical profiles. The height of the aerosol mixed layer was determined by finding the local minimum of the derivative of the backscatter signal that was closest to the surface. The urban boundary layer was also examined over Mexico City using a scanning backscatter lidar to study the structure of the atmosphere (Cooper and Eighinger 1994). During this experiment, the lidar was able to observe structures in the boundary layer including low-level jets, thermal plumes, convective eddies, and entrainment into the planetary boundary layer.

For a preliminary study, the lidar was placed at SJSU in downtown San José. Observations of vertical velocity on 24 September 2011 showed a stable boundary layer with little vertical motion in the early morning (Fig. 6a). Before 900 PST, a cold front moved through the region and brought in cleaner air, which led to a decrease in the height of the aerosol layer to 500 m AGL (Fig. 6b). Around 1030 PST, convective thermals developed due to heating at the surface and increased mixing in the surface layer. By the

afternoon the surface layer height increased to 1000 m AGL (Fig. 6c). The next day, clouds allowed for the surface layer height to remain ~1000 m AGL (Fig. 7a). The cloud cover kept the convective thermals weaker in strength than the day before as there was less surface heating. At 1230 PST, downdrafts were observed from ~1000 to 2000 m AGL as slight precipitation occurred but did not reach the ground (Fig. 7b).

Observations on 3 November 2011 showed a convective boundary layer that developed in the late morning (Fig. 8). Regions of vertical velocities of ~3 m s^{-1} were discovered from the lidar observations at 0915 PST (Fig. 8a). The regions of positive buoyancy are a result of heating at the surface, producing convective updrafts. The height of the boundary layer was at 1800 m AGL (Fig. 8a).

Later in the afternoon, an increase in frequency and strength of the convective thermals was observed (Fig. 8b) due to an increase of heating at the surface. Also, convective updrafts of ~4 m s^{-1} lead to a growth of the boundary layer to 2000 m AGL (Fig. 8b). This preliminary study found that the lidar was able to resolve certain boundary layer structures such as convective thermals. Therefore, the lidar is capable of resolving circulation patterns in the atmosphere around a fire that are of the same scale.

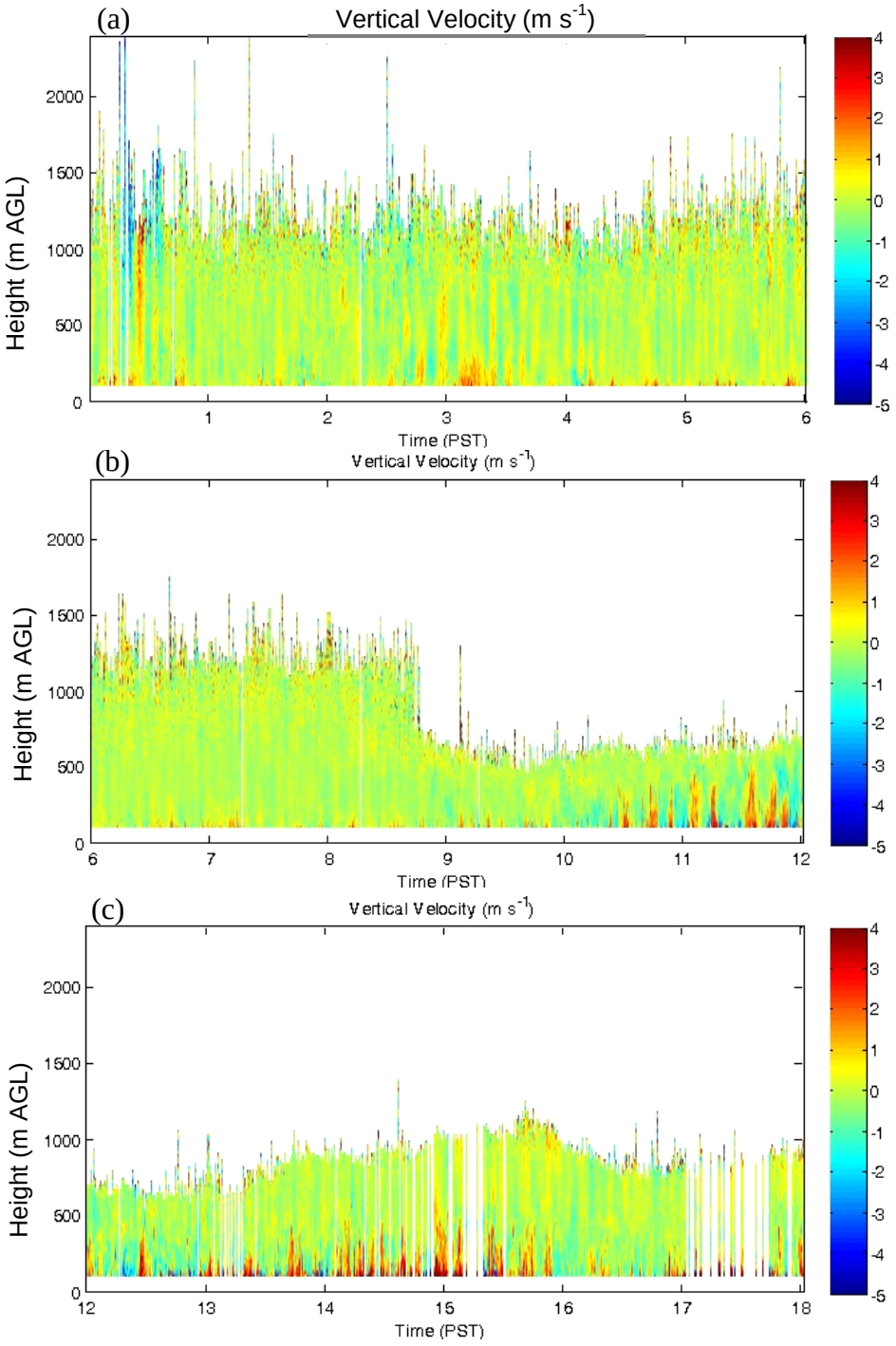

Fig. 6. Vertical velocity (m s^{-1}) profiles over time from lidar located on the top of a building in downtown San José on 24 September 2011.

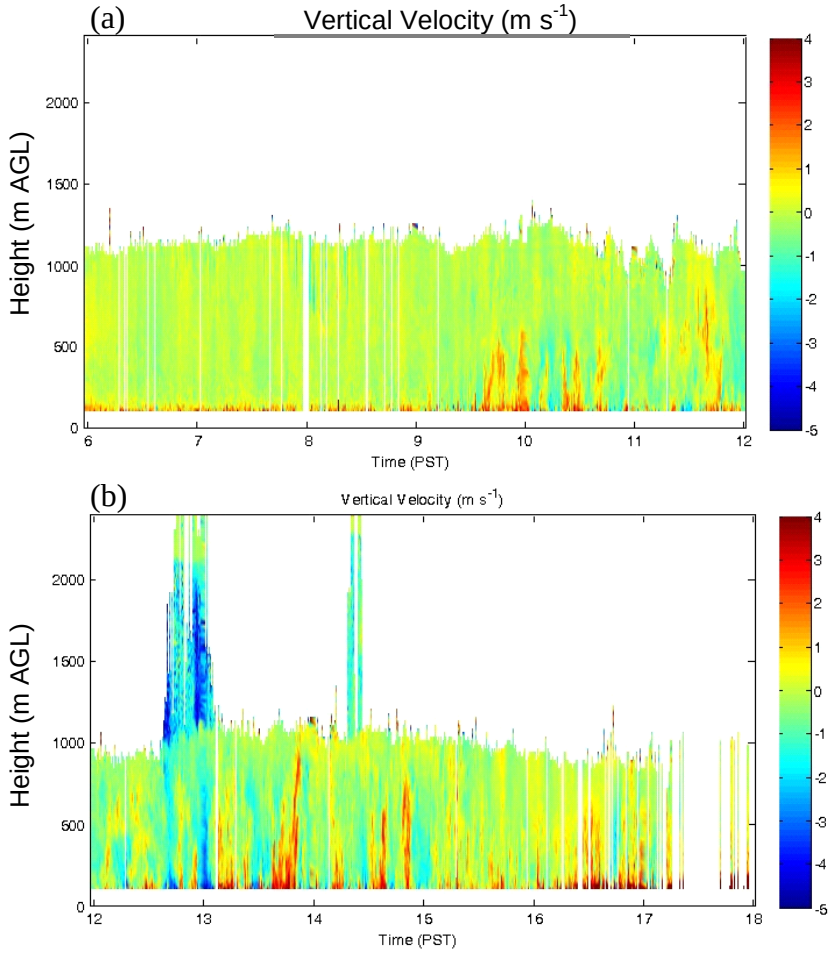

Fig. 7. Vertical velocity (m s^{-1}) profiles over time from lidar located on the top of a building in downtown San José on 25 September 2011.

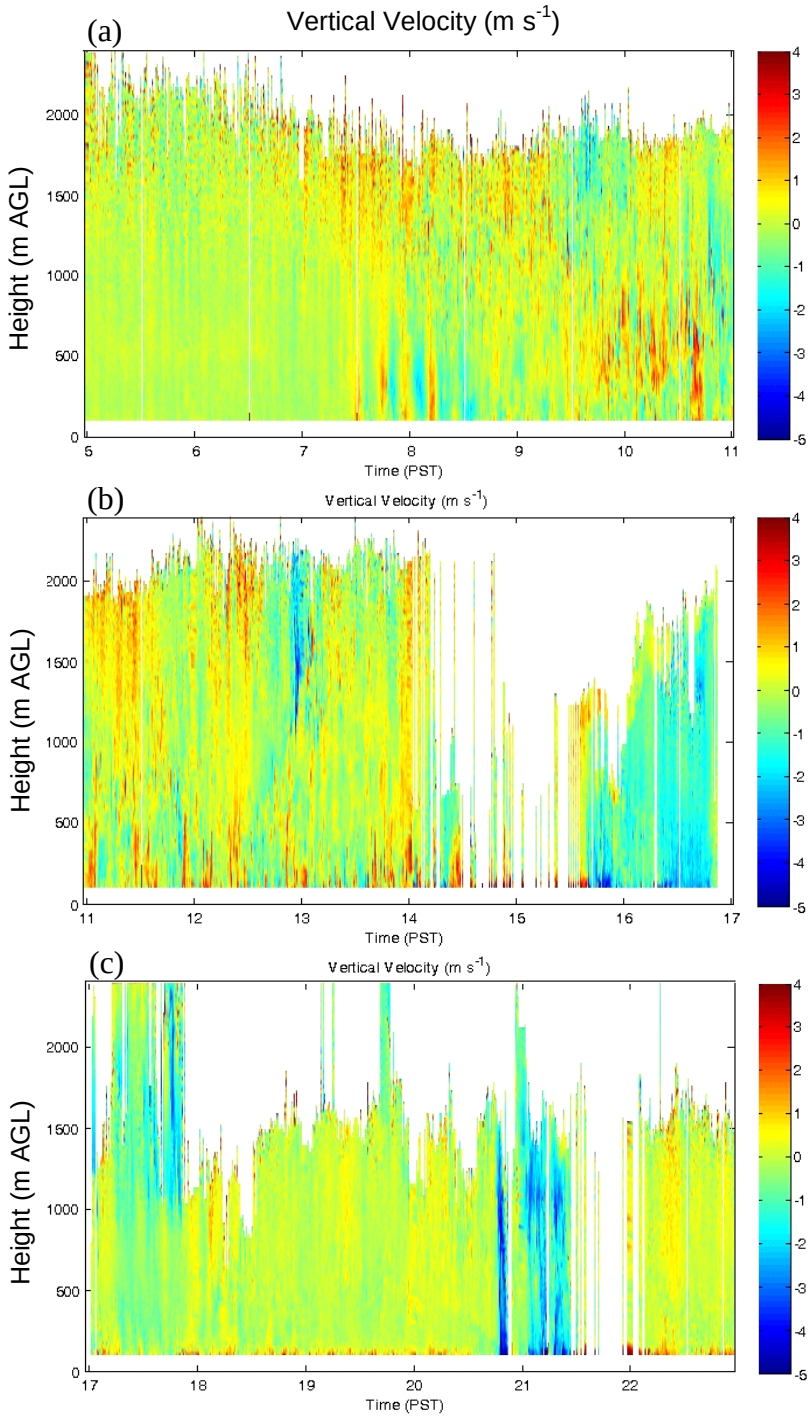

Fig. 8. Vertical velocity (m s^{-1}) profiles over time from lidar located on the top of a building in downtown San José on 3 November 2011.

2) Along-valley Winds

A preliminary study was conducted to test the lidar performance in areas of complex terrain. The lidar was deployed in a mountain valley with a depth of ~400 m east of San José on 9-10 April 2011. Various scanning techniques were used to test the scanning capabilities of the lidar. An RHI scan was performed with the lidar located at the valley floor, scanning along the valley at an azimuth angle of 150^{o} with elevation angles ranging from 0^{o} to 80^{o}. The backscatter intensity from the scan (Fig. 9a) shows a small area of high backscatter intensity at 700 m along the surface. When compared with a map of the terrain, the area of high backscatter intensity corresponds to the location where the lidar beam was hitting the terrain. Therefore, any data behind this location is invalid as it is past the terrain. Future scans used a different azimuth angle to avoid the terrain and optimize the data collected. Also, the elevation angle can be adjusted from 5^{o} to 10^{o} in order to avoid hitting the terrain.

After adjusting the scanning routine, observations were made throughout the two-day study. Radial velocities range between 3 and 8 m s^{-1} at 1738 PST and were uniform throughout the boundary layer, indicating a coupling of the atmosphere in the valley and the atmosphere above the valley (Fig. 10a). There were fairly uniform wind speeds due to mixing in the convective boundary layer (Whiteman 2000).

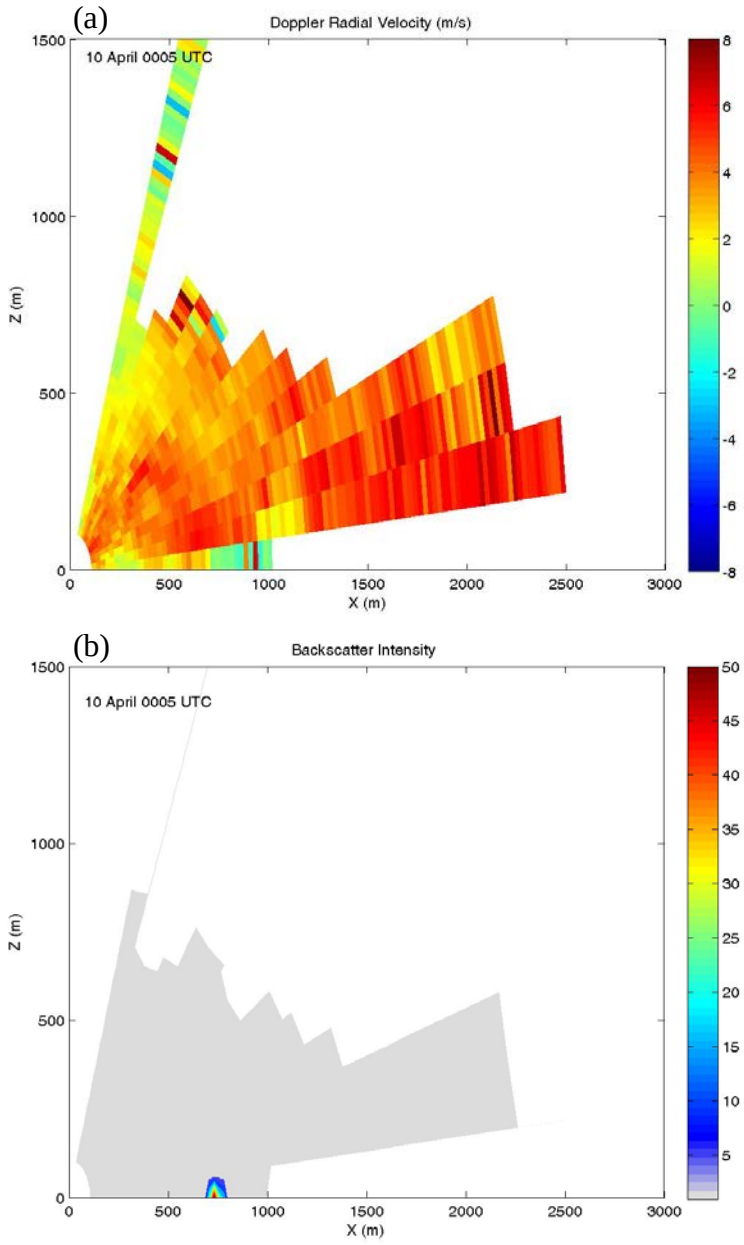

Fig. 9. RHI lidar scans of the valley atmosphere along a 150^{o} azimuth angle and elevation angles varying from 0^{o} to 85^{o} by increments of 5^{o}. The lidar was located at the origin (0,0). (a) The backscatter intensity (SNR+1), (b) radial velocity (m s^{-1}) where positive values represent flow away from the lidar and negative values represent flow towards the lidar.

The convective thermals that rise from the valley floor, indicated in the vertical velocity profiles, characterize a coupled period (Fig. 11a). The sounding launched from the valley floor indicated the height of the boundary layer at 600 m AGL with fairly uniform wind speeds above the ridgetop (Fig. 12). At 2000 PST, the boundary layer depth decreased slightly to 550 m AGL (Fig. 13). In the RHI scan at the same time, there was a region of increased velocities within a layer from 100-400 m (Fig. 10b). During the evening transition period, the atmosphere in the valley became decoupled from the atmosphere above the valley due to the buildup of the stable inversion layer. There was also a transition from up-valley to down-valley winds. Vertical velocities during this time were weaker than in the afternoon (Fig. 11b). At midnight, surface winds near the valley floor were calmer with velocities between 0 and 2 m s^{-1} (Fig. 10c). At 0302 PST, the velocities decreased to between -2 and 0 m s^{-1} as the winds transitioned from up- to down valley and winds aloft remained slightly higher (Fig. 10d).

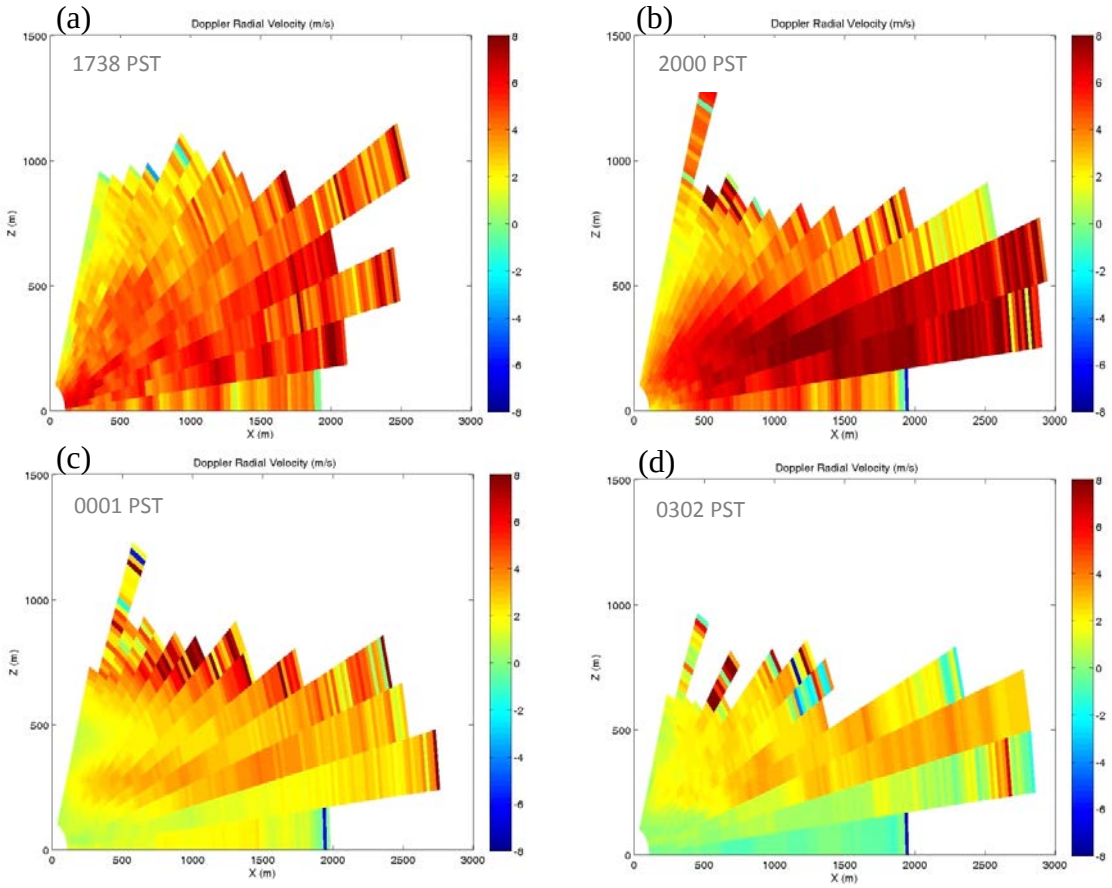

Fig. 10. RHI lidar scans along the valley atmosphere along a 145^{o} azimuth angle and elevation angles varying from 0^{o} to 80^{o} by increments of 5^{o} on 9-10 April 2011. The lidar was located at the origin (0,0). The radial velocity (m s^{-1}) displays the positive values representing flow away from the lidar and negative values representing flow towards the lidar.

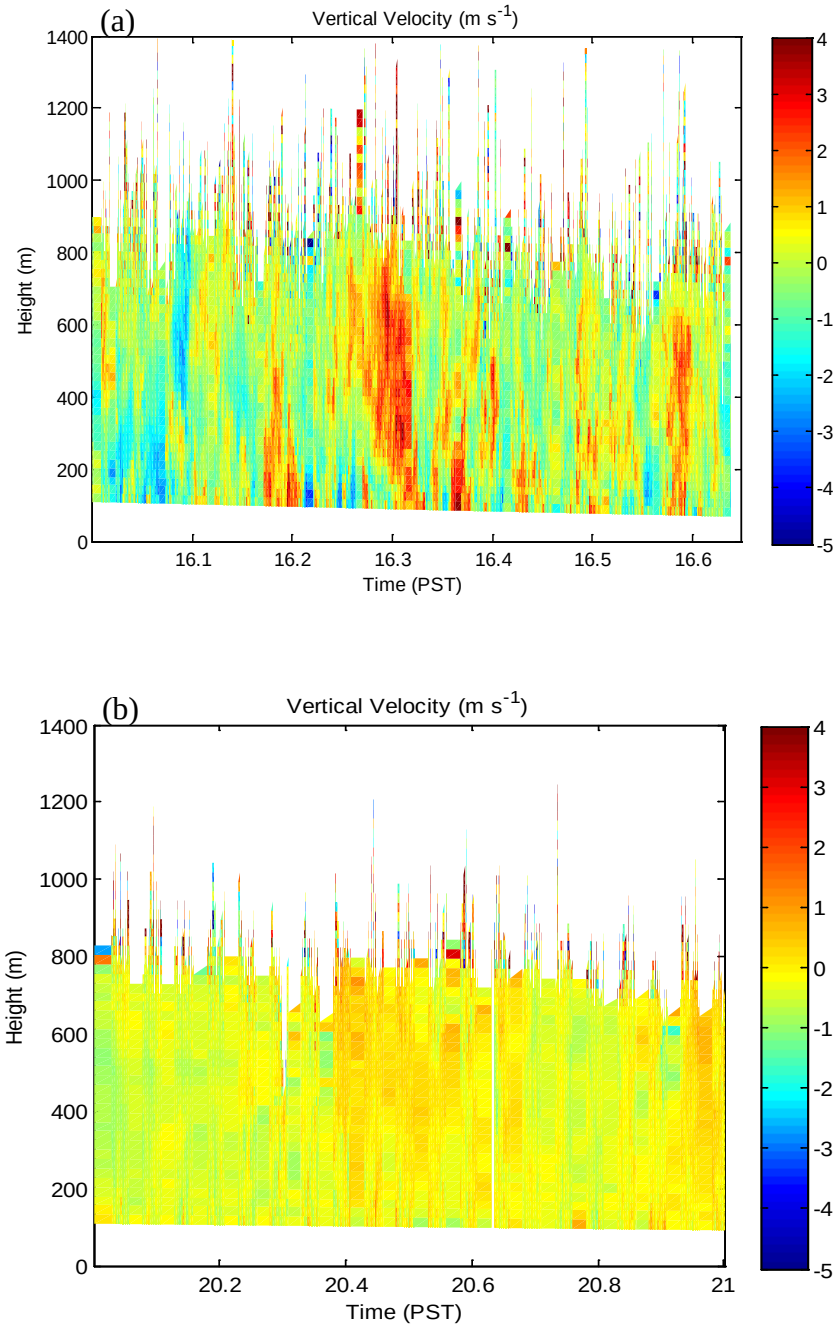

Fig. 11. Vertical velocity profiles over time from lidar located on valley floor on 9 April 2011.

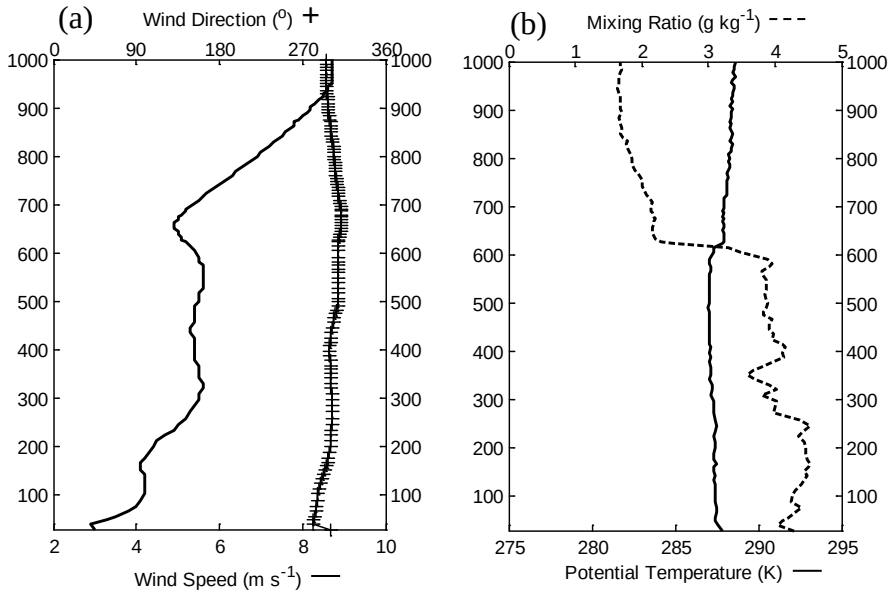

Fig. 12. Radiosonde sounding launched from the valley floor at 1600 PST on 9 April 2011 with profiles of (a) wind speed and direction and (b) potential temperature and mixing ratio (dashed).

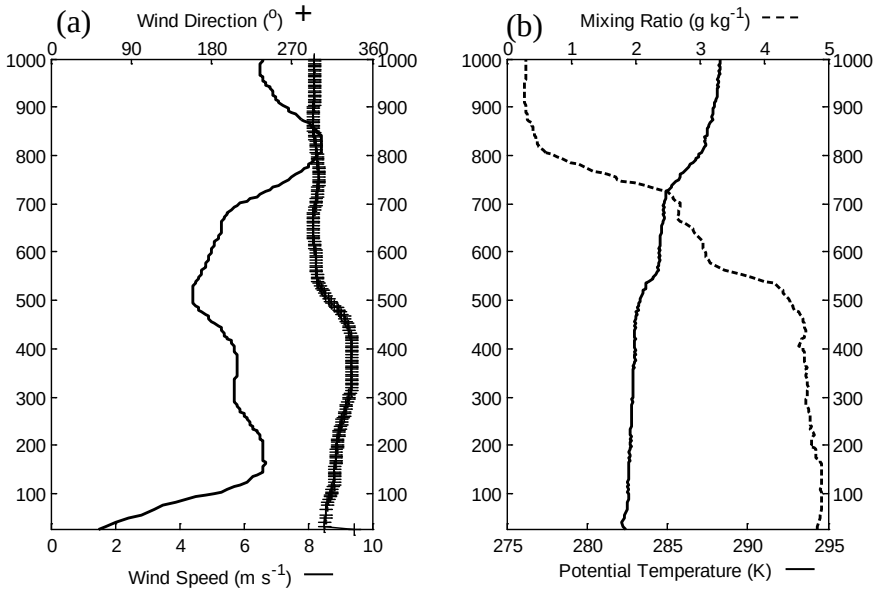

Fig. 13. Radiosonde sounding launched from the valley floor at 2000 PST on 9 April 2011 with profiles of (a) wind speed and direction and (b) potential temperature and mixing ratio (dashed).

By the next morning at 0600 PST, as indicated from the sounding, an inversion had developed overnight in the valley (Fig. 14). Cooling at the valley floor can be created by a combination of the development of downslope winds bringing cooler air to the valley bottom and the loss of longwave radiation at night. The lidar scans at 0557 PST show the surface winds along the valley ranged between -2 and 2 m s^{-1}, while the velocities aloft were stronger (Fig. 15a). During the night, as the inversion developed in the valley, the winds at the valley floor became calm. The valley atmosphere at this time was decoupled from the free atmosphere due to the suppression of vertical exchange of air by the stable boundary layer. In the residual layer above the ridgetop level, winds were still influenced by the synoptic conditions and were stronger than in the valley (Whiteman 2000). Stronger winds aloft were also observed in the sounding at 500 m AGL (Fig. 14b). After sunrise, the velocities within the boundary layer increased slightly while winds above were between -4 and -2 m s^{-1}. This region of reversed velocities at 500 m AGL is a characteristic of the stable core, which is the remnant of the nighttime inversion (Whiteman 1982). Due to the development of the convective boundary layer, the stable core separated from the surface, and winds within the boundary layer accelerated (Whiteman 2000). As the convective boundary layer developed, increased vertical velocities were observed in the lower boundary layer as there was increased mixing in the atmosphere (Fig. 16b).

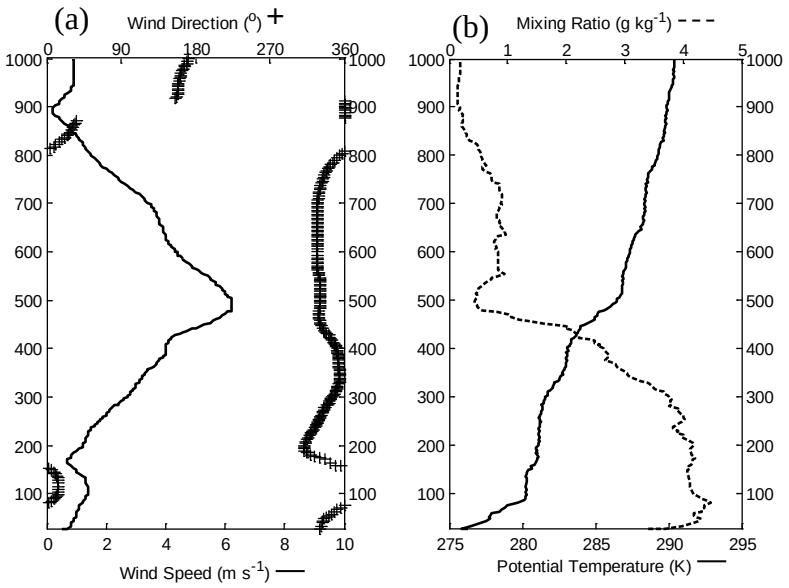

Fig. 14. Radiosonde sounding launched from the valley floor at 0600 PST on 10 April 2011 with profiles of (a) wind speed and direction and (b) potential temperature and mixing ratio (dashed).

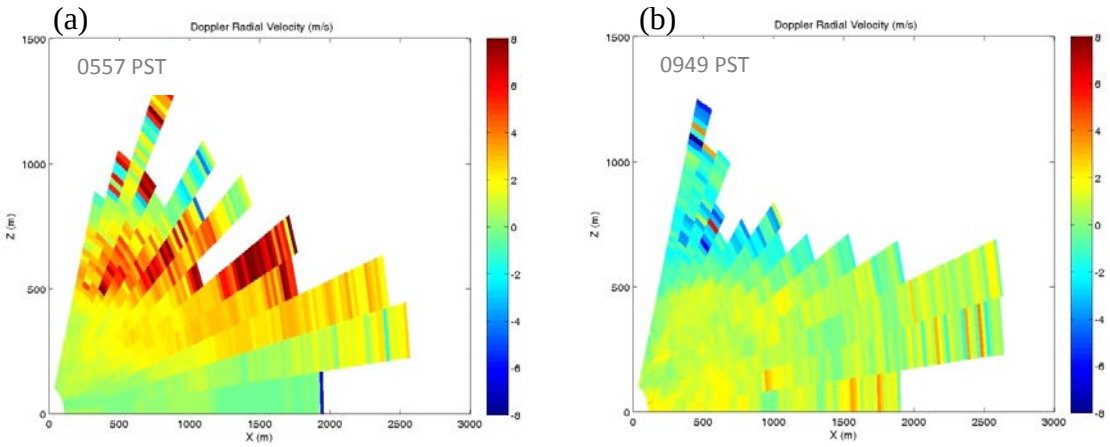

Fig. 15. RHI lidar scans along the valley atmosphere along a 145^{o} azimuth angle and elevation angles varying from 0^{o} to 80^{o} by increments of 5^{o} on 10 April 2011. The lidar was located at the origin (0,0). The radial velocity (m s^{-1}) displays the positive values representing flow away from the lidar and negative values representing flow towards the lidar.

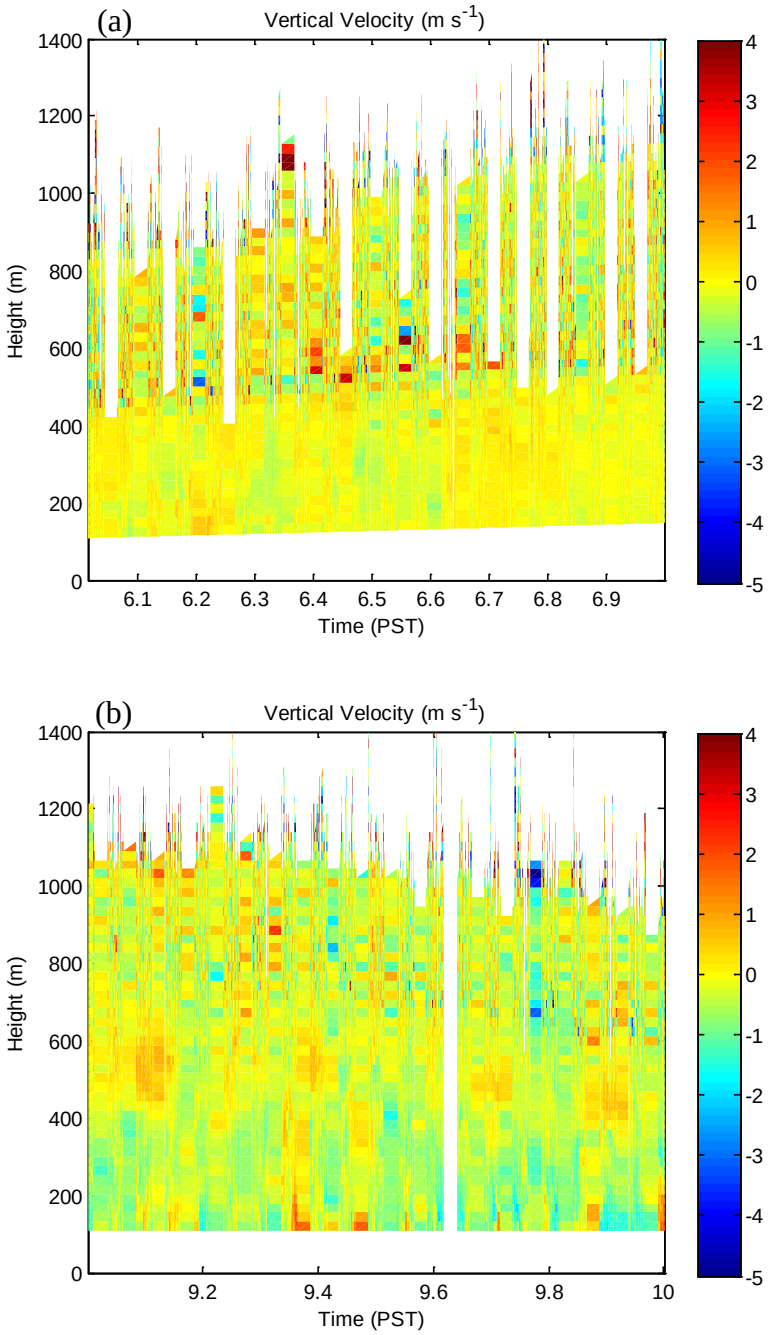

Fig. 16. Vertical velocity profiles over time from the lidar located on the valley floor on 10 April 2011.

This preliminary study found a good agreement between the lidar and radiosonde measurements in determining the boundary layer height, thus validating the lidar measurements. The preliminary studies provided practice for using lidar techniques in the field and for arranging scanning strategies to optimize the data collected.

b. Thermodynamic Plume Properties

In order to examine the vertical thermodynamic structure within the plume, two radiosondes were launched from downwind and into the plume after the fire was ignited. At 1237 PST, the potential temperature was 298.8 K at the surface decreasing to 294.5 K in the mixed layer, which extended from 80 m to the top of the boundary layer at 440 m AGL (Fig. 17a). This indicates a warming of ~4 K within the lowest layers of the plume. Water vapor mixing ratio at the surface was 7 g kg^{-1}, and increased ~1 g kg^{-1} at 80 m AGL. Enhanced moisture is expected within the plume due to the release of water vapor as a by-product of combustion (Potter 2005). These measurements are comparable to measurements found by Kiefer et al. (2012), who observed an increase in potential temperature within a wildland fire plume of 3-5 K and an increase in mixing ratio of 0.5-3.5 g kg^{-1}. Mixing ratio observations of 2 g kg^{-1} were found by Clements et al. (2006) and are slightly higher than observations from this study as a result of different types of fuels burned during the experiments. Radiometer measurements from downwind of the burn unit do not show the same characteristics seen in the radiosonde measurements in the plume, indicating that increased moisture is due to combustion from the fire and release of water vapor (Fig. 17b).

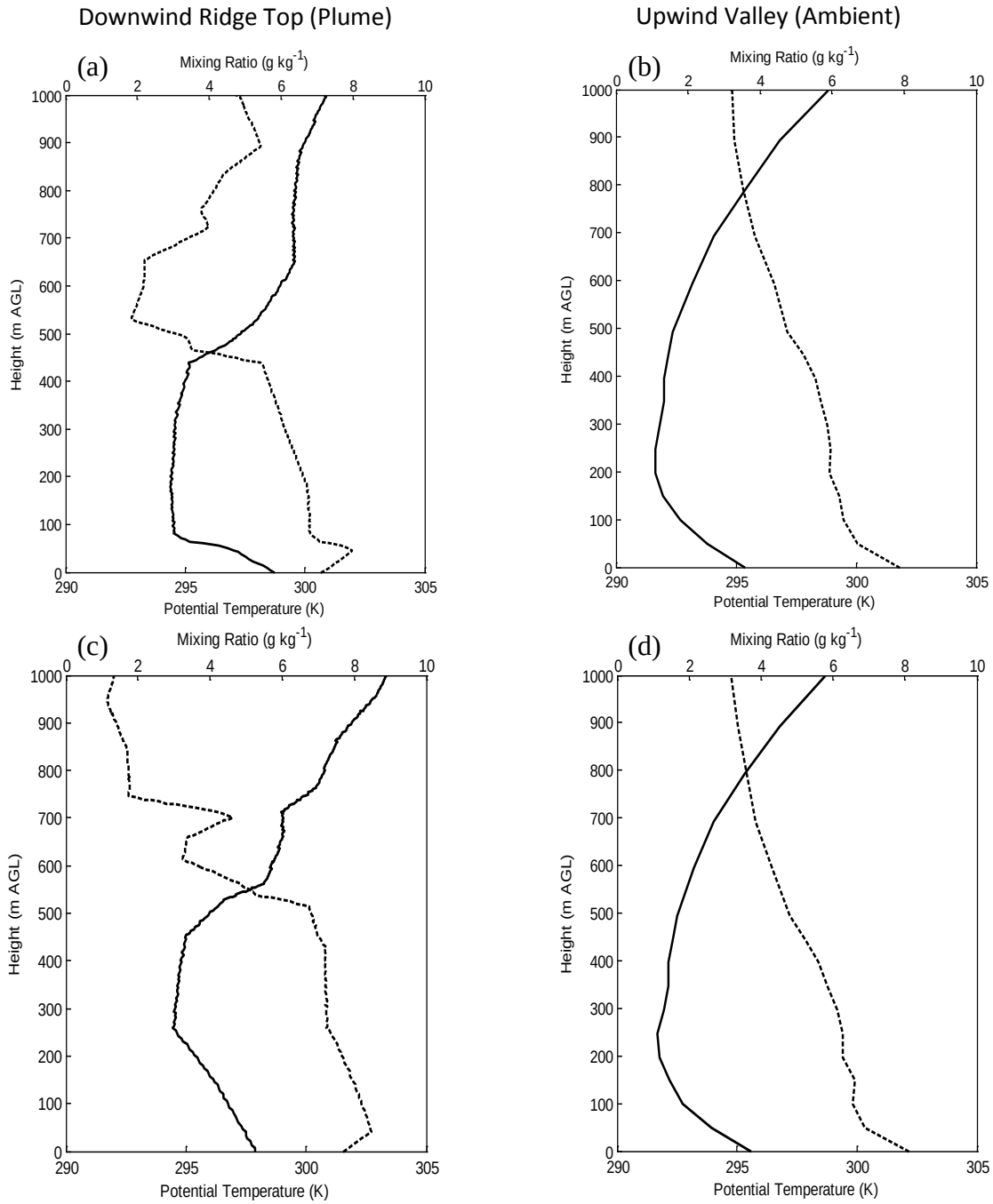

Fig. 17. Water vapor mixing ratio and potential temperature profiles from radiosonde launched from the ridge top location at 1237 PST (a) and 1644 PST (c) and profiles from the radiometer (b,d) at the same times on 13 July 2011.

After the fire moved farther west into the burn unit at 1644 PST, another radiosonde was launched into the plume from the top of the ridge. Increased heating and turbulence during the day led to mixing in the boundary layer, and the height of the surface layer increased to 220 m AGL. The potential temperature at the surface was 3.5 K warmer than at the height of the surface layer (Fig.17c). The mixing ratio at the surface was 8 g kg^{-1} and increased to 8.5 g kg^{-1} at 80 m. The enhanced moisture of 0.5 g kg^{-1} above ambient was observed within the plume, which was less than observed earlier in the day as the fuels had dried out by the afternoon and there was less available moisture.

c. Fire-induced Circulations

In order to obtain observations of the kinematic structure within and near the plume, a suite of scanning strategies were scheduled for the lidar. Around 1700 PST, the fire line moved farther west and closer to the location of the lidar. The observations showed that the lidar was able to scan through even the most intense areas of the plume (Fig. 18). The regions of high backscatter intensity correspond to areas with high smoke density or the convection core of the plume. In some scans, there were multiple convection cores observed due to the burn strategies of the fire crews to ignite in multiple lines. Multiple convection cores are commonly observed during both wild and prescribed fires and in simulations (Kiefer et al. 2009). It has been suggested that the large temperature anomalies produced by a fire generate atmospheric circulations, which play a role on the development of individual convection cores (Kiefer et al. 2009).

Regions of lighter and slightly reversed radial velocities were observed near the 30^{o} azimuth scan angle due to the geometry of the scan. The lidar measures radial velocity along the beam; therefore, with the ambient wind from the northwest, the radial velocity component will be weaker as it is more perpendicular to the ambient wind speed.

At 1000 m east and 450 m north of the lidar position (Fig.18a), the scan captured an area of increased radial velocities to ~8 m s^{-1} south of the plume, indicating horizontal acceleration of the wind into the updraft region. Directly downwind of the plume, there was a smaller region of decreased velocities of 0 to 1 ms^{-1}, indicating the formation of a convergence zone. The development of a convergence zone has also been observed by Clements et al. (2007) downwind of a grass head fire. Convergence zones associated with fire were observed on a larger scale by Banta et al. (1992). However, Banta observed a reversal in the velocities, indicating that a circulation had developed within the plume. To better determine the magnitude of the convergence zone, the radial velocity along one azimuth angle of the scan that is south of the region of the plume is analyzed (Fig. 19a). An increase in radial velocity of ~5 m s^{-1} was observed with a sharp decrease of ~1 m s^{-1} along the lidar beam indicating the location of the convergence zone at 1100 m, which is about 200 m downwind of the fire front. In addition, an area of reversed radial velocities between -2 and 0 m s^{-1} was observed to the northeast of the plume, indicating a rear surface inflow into the fire's head. This flow reversal was also observed during the Fireflux experiment (Clements 2007).

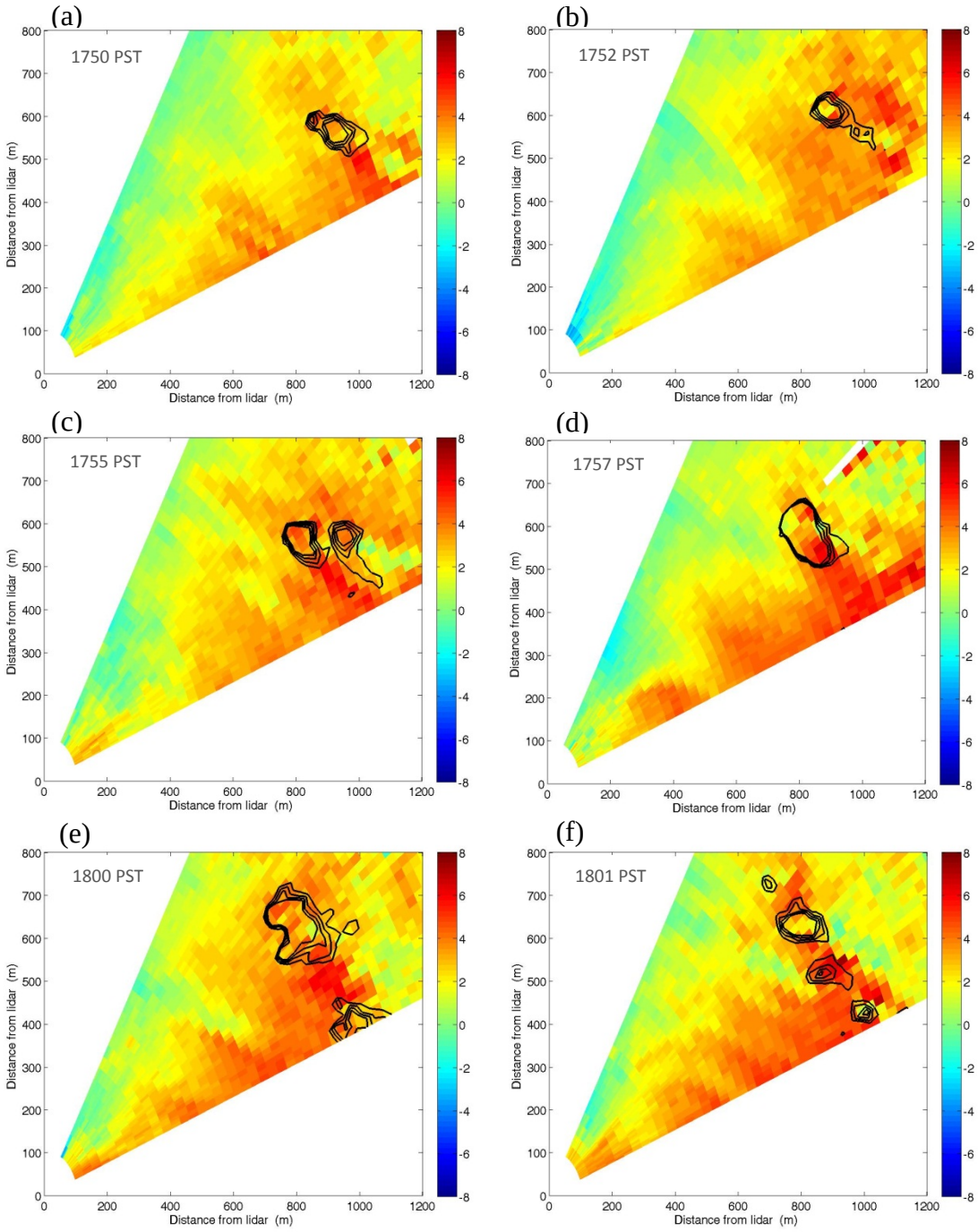

Fig. 18. PPI lidar scans through the plume at specified times with the lidar located at the origin (0,0). An elevation angle of 10^{o} was used with azimuth angles ranging between 30-70^{o} in increments of 1.0^{o}. The images display the radial velocity component (m s^{-1}). The black contours outline the areas of high backscatter intensity indicating the location of the plume. Contours are shown from 3.0 to 6.0 by intervals of 1.0 SNR +1.

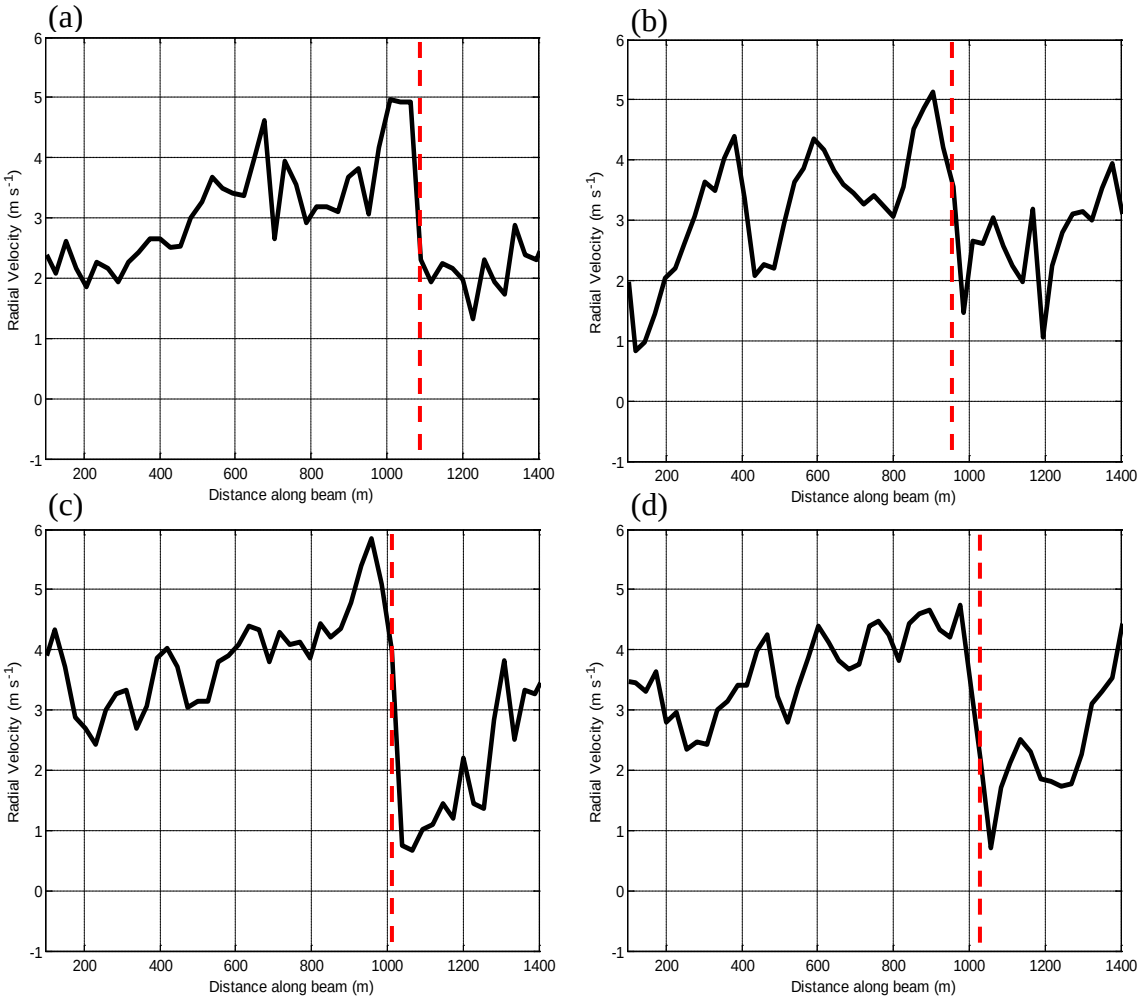

Fig. 19. Doppler radial velocity at (a) 1750 PST on 13 July 2011 for a 10^{o} elevation angle and an azimuth angle of 68^{o} (b) at 1757 PST of 62^{o} (c) at 1800 PST of 65^{o} and (d) at1801 PST of 64^{o}. The location of the convergence zone is indicated by the red dashed line.

The fire-induced acceleration of the wind into the base of the plume was caused by a horizontal pressure gradient that was created by low pressure that developed downwind of the fire front. The low pressure ahead of the fire produced a fire-induced wind into the fire front. In addition, acceleration of surface winds into the plume base was observed (Fig. 18) to occur on both the upwind and downwind side in some instances

with a deceleration in velocities downwind of the convection cores. Coen et al. (2004) also observed the horizontal acceleration into the base of the convective updraft, although on a larger scale during a wildfire event. The magnitude of the horizontal acceleration was much higher in the study by Coen et al. due to the difference in the intensity and strength of the inflow of prescribed fires versus wildfires. The wildfire observed by Coen et al. was in forest fuels which typically burn more intensely given the higher fuel loads.

Later at 1752 PST, the convection core progressed to the northwest with the plume extending towards the southeast (Fig. 18b). A similar region of decreased radial velocities was observed downwind of the plume with an adjacent region of increased velocities. At 1755 PST, the fire developed two convection cores (Fig. 19c). There was a region within a larger convection column extending south of the plume with increased velocities of 4 to 6 m s^{-1}. By this time, the region directly downwind of the plume had a decrease in velocities by 3-5 m s^{-1}. The region spread over a larger area than in previous scans showing an extension of the convergence zone 200 m downwind of the plume. At 1757 PST, the area of high backscatter intensity increased as the two convection cores combined into one large region (Fig. 18d). The region of decreased velocities was still observed downwind, however, the region of accelerated velocities included a larger area south of the plume. The along-beam velocity showed a sharp decrease in velocities occurring around 950 m (Fig. 19b). Also, a region of high velocities reaching 8 m s^{-1} was observed in the southeast region of the plume, while there was a region of velocities between 0 to 2 m s^{-1} in the northwest region of the plume. This indicates a convergence zone also occurred within the plume. Banta et al. (1992) also observed a similar

structure, however with reversed velocities in the plume indicating a rotation or vorticy forming within the plume.

At 1800 PST, fire crews began firing along the southeast region of the burn unit as indicated by another region of high backscatter intensity that developed near the bottom of the lidar scan (Fig. 18e). A convergence zone was observed downwind of the larger convection column by a clearly defined line separating the high and low radial velocities. The radial velocity over the 65^{o} azimuth angle showed a sharp deceleration of the wind from 6 m s^{-1} to 1 m s^{-1} within a distance of about 100 m (Fig. 19c). At 18:01 PST, multiple convection columns were observed with several distinct regions of high backscatter intensity (Fig. 18f). The decrease in the radial velocity of 4 m s^{-1} was observed at the convergence zone. The convergence zone again, extended downwind of the main convection column parallel to the ambient wind direction. The consistent presence of the region of weak radial velocities downwind of the convection core indicated that convergence is less transient and most likely played a major role in the development of near-surface fire-induced circulations that drove the fire spread. Farther downwind from the plume, there was also a decrease in wind speed measured from the sodar (Fig. 20). The winds after this time then increased to 5.6 m s^{-1}, also indicating a convergence zone had developed downwind of the plume.

The divergence of the radial velocity, δ_r, was calculated for the lidar scans using the following equation:

$$\delta_r = \frac{\partial V_r}{\partial r} \qquad (2)$$

where V_r is the radial velocity and r is the range distance along the lidar beam. In lidar scans, the regions of greater negative divergence, or convergence, correspond to the location of the convergence zone that was found previously. The calculated values of divergence of the radial velocity were between -0.04 s^{-1} and -0.06 s^{-1} in the convergence zone region.

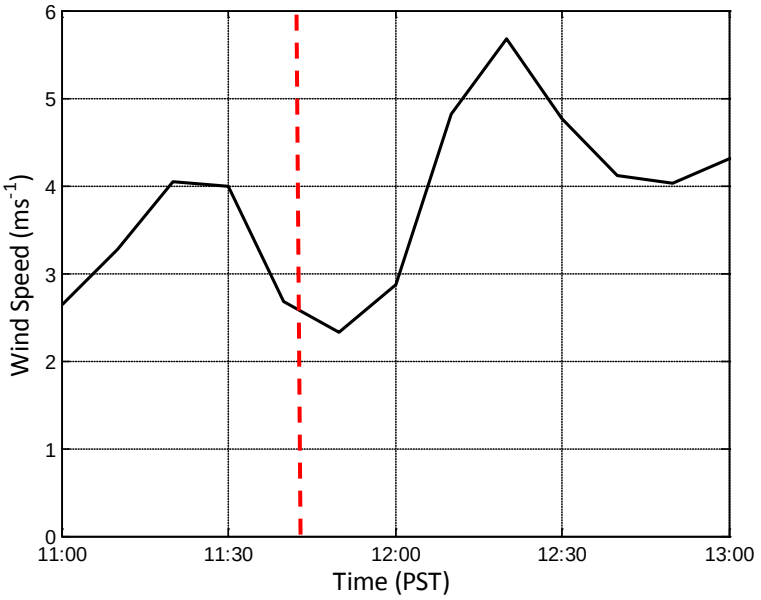

Fig. 20. 10 min averaged wind speeds measured at 20 m AGL from the sodar. Red dashed line indicates the time the fire was ignited.

In the vertical cross-section scans of the plume, there was acceleration beneath the plume with weaker velocities aloft (Fig. 21a-d). This indicates a strong indraft into the base of the convection column occurring within the plume, as also observed in Coen et al. (2004). These strong inflows also indicate a recirculation of air into the fire front. The magnitude of the radial velocity increased as the area of the plume enlarged, indicating

that the winds accelerated as the fire became more intense. Velocities above the surface at 500 m AGL were slower ahead of the plume and then accelerated in the region of the plume, indicating upper-level divergence (Fig. 21a).

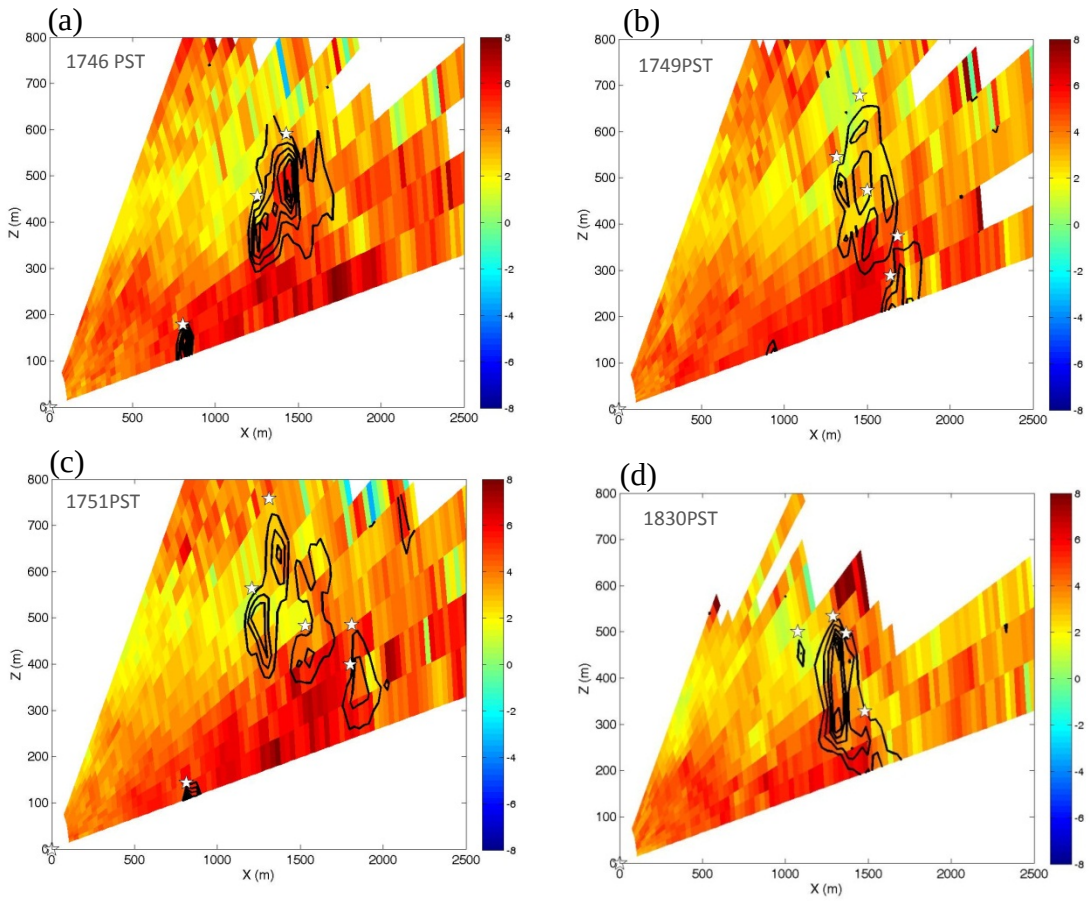

Fig. 21. RHI lidar scans through the plume along a 95^{o} azimuth angle at specified times with the lidar located at the origin (0,0). The images show the radial velocity component (m s^{-1}) with the positive values representing flow away from the lidar and negative values representing flow towards the lidar. The black contours indicate areas of high backscatter intensity displaying the location of the plume. Contours are shown from 0.0 to 3.0 by intervals of 0.25 SNR +1.

At 1749 PST, the radial velocities beyond the plume boundary decreased slightly, indicating a convergence zone below the convection column of the plume that extended vertically nearly 150 m (Fig. 21b). The deceleration was also observed at 1830 PST, extending vertically 300 m (Fig. 21d). The vertical extent of the convergence zone observed by Banta et al. (1992) extended ~1 km above the surface.

Observations from previous studies have identified the location of a convergence zone ahead of a propagating fire front. Clements et al. (2007) observed a short-lived convergence zone ahead of the fire front, whereas Banta et al. (1992) found a convergence pattern downwind related to a downwind line of cumulus congestus clouds that formed. A coupled fire-atmosphere model found the convergence pattern to be connected with the downwind tilt of the plume (Clark et al. 1996). The development of the convergence zone is connected to the heating from the fire that causes convective updrafts within the plume. Markowski and Richardson (2010) suggest that a positive pressure perturbation exists above a warm bubble (a plume for this study) because the rising warm air laterally pushes air above it out of the way, leading to upper-level divergence. This causes a negative pressure perturbation to develop at the surface, allowing for the formation of the convergence zone beneath the plume. Therefore, the location of the convergence zone, relative to the fire, is dependent on the strength and direction of the ambient wind speed. The dashed line in Fig. 21a-d indicates the location of the plume height found using the algorithm described in Section 3c. As noted by Sofiev et al. (2012), plume injection-heights occur mostly in the atmospheric boundary layer. A linear relation between plume height and fire intensity was observed from

different field experiments (Lavoué et al. 2000). At 1746 PST the maximum plume height was at 600 m AGL and increased to 680 m after 3 min, indicating little vertical development within the plume (Fig. 21a-b). At 18:30 PST the plume height decreased to 550 m as the plume dispersed (Fig. 21d). Multiple regions of high backscatter intensity are shown within the plume, and the algorithm is able to identify the location where the maximum gradient of the backscatter occurs.

d. Plume Turbulence

In order to examine the turbulent structure downwind of the fire, 10 min averaged vertical profiles of vertical velocity and turbulent kinetic energy (TKE) were evaluated from the sodar. Using the turbulence statistics from the sodar, profiles of the TKE were calculated. After the ignition at 1143 PST, there is downward motion that develops downwind of the fire as the air is recirculated to the surface (Fig. 22a). Throughout the burn, there are fluctuations between updrafts and downdrafts that occur with a maximum in upward velocity of 1.1 m s^{-1}. Upward vertical velocities are due to the buoyancy from the combustion of the fuels, however the magnitude of the updrafts downwind are less than observed at the fire front where the strongest convection occurs.

Some stronger updrafts or regions of subsidence could not be identified due to the 10 min averaging period of the sodar. Overturning in the plume develops and the air recirculates towards the surface. The greatest values of TKE of 2.9 m^2 s^{-2} are observed in the transition regions from upward to downward motion (Fig. 22b) as the shift in the vertical velocity from upward to downward leads to the overturning of air and

entrainment within the plume. TKE values on the day of the burn were slightly higher than the day before under the same synoptic conditions (not shown); indicating that the turbulence in the lower boundary could be a result of increased mixing from the fire.

Throughout the day, crews continued the fire line so that the fire progressed towards the west and away from the location of the sodar. Throughout the afternoon as the convection core of the fire moved farther away from the sodar, the magnitude of the vertical velocity decreased to ±0.5 m s^{-1} and the TKE decreased as well to 0 and 1 m^2 s^{-2} (Fig. 22c-d). In the evening, the magnitude of the TKE still remained low, however at times there were periods of increased TKE as a result of smoldering from the fire.

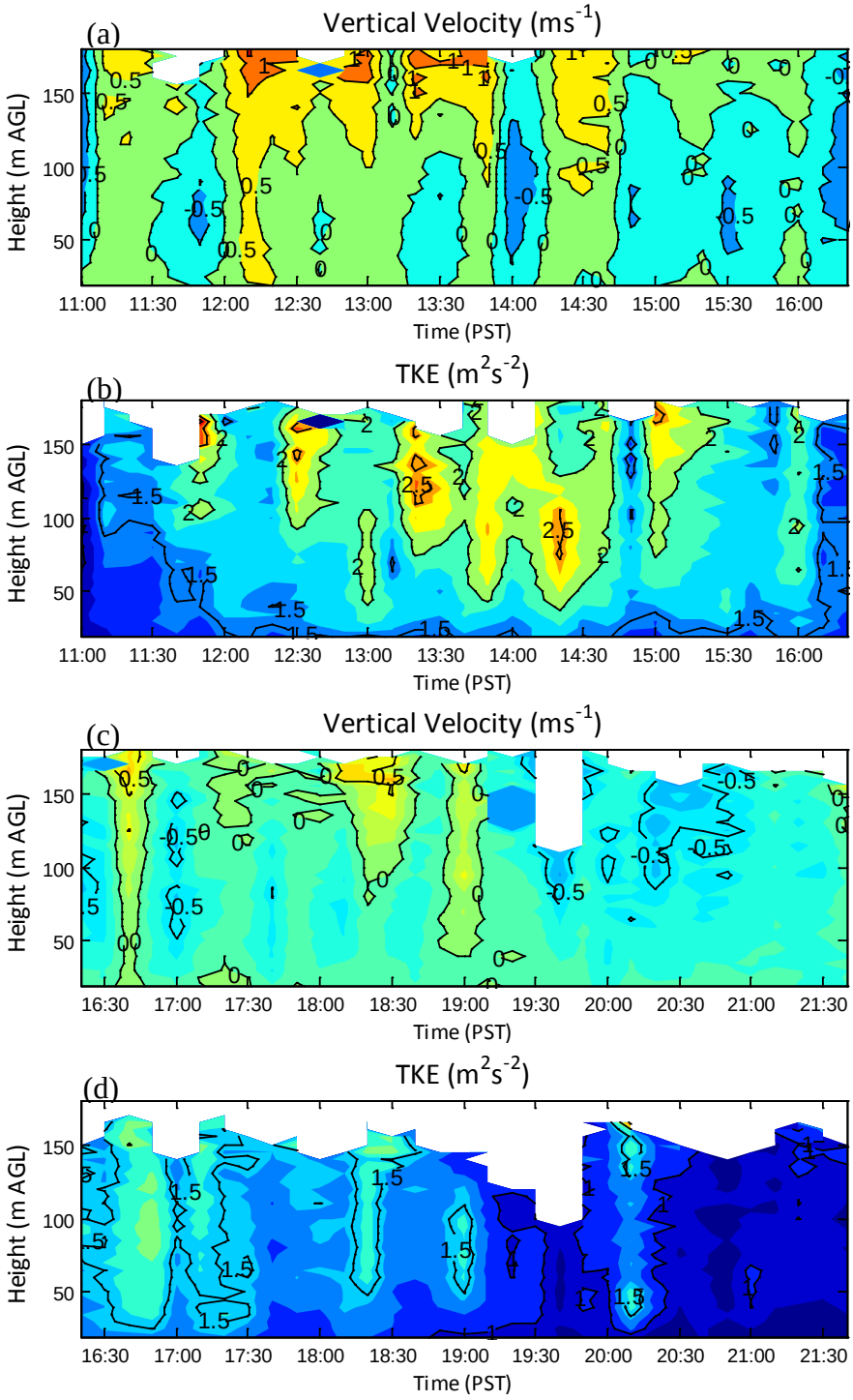

Fig. 22. Time-height contours of vertical velocity (a,c) and turbulence kinetic energy (b,d) measured from the sodar on 13 July 2011 from the ridgetop location.

e. Convection Core Tracking

In order to examine the development of the fire over time, two methods were used to characterize the movement of the fire and the plume by analyzing 90 min of scans with 150 s between scans. As discussed earlier, the maximum region of backscatter intensity of a PPI scan indicates the location of the convection core. This region can also be identified as the location of the fire front because it is where there is the highest smoke density. The first method determines the fire spread rate by tracking the location of the maximum backscatter intensity of each scan and calculates the distance the convection core moves between scans. The movement of the fire can be seen in Fig. 23a-b by the shift in the location of the maximum backscatter intensity. The average calculated fire spread rate using this method was found to be 0.67 m s^{-1}.

The second method follows the plume boundary between scans to calculate the movement of the plume over time. The algorithm, described in Section 3c, was able to successfully determine the boundaries of the smoke plume. The movement of the plume over time found from this method was 2.4 m s^{-1}. In some regions where the intensity was weak, the algorithm was not able to determine the boundary as well. In Fig. 23c, there is a small region of backscatter intensity southeast of the main convection column that was not identified by the algorithm. This occurs when the difference of the intensity at that point and the surrounding area is not as great as in the difference in the region of the convection core. Therefore, the algorithm will not characterize this region as a boundary.

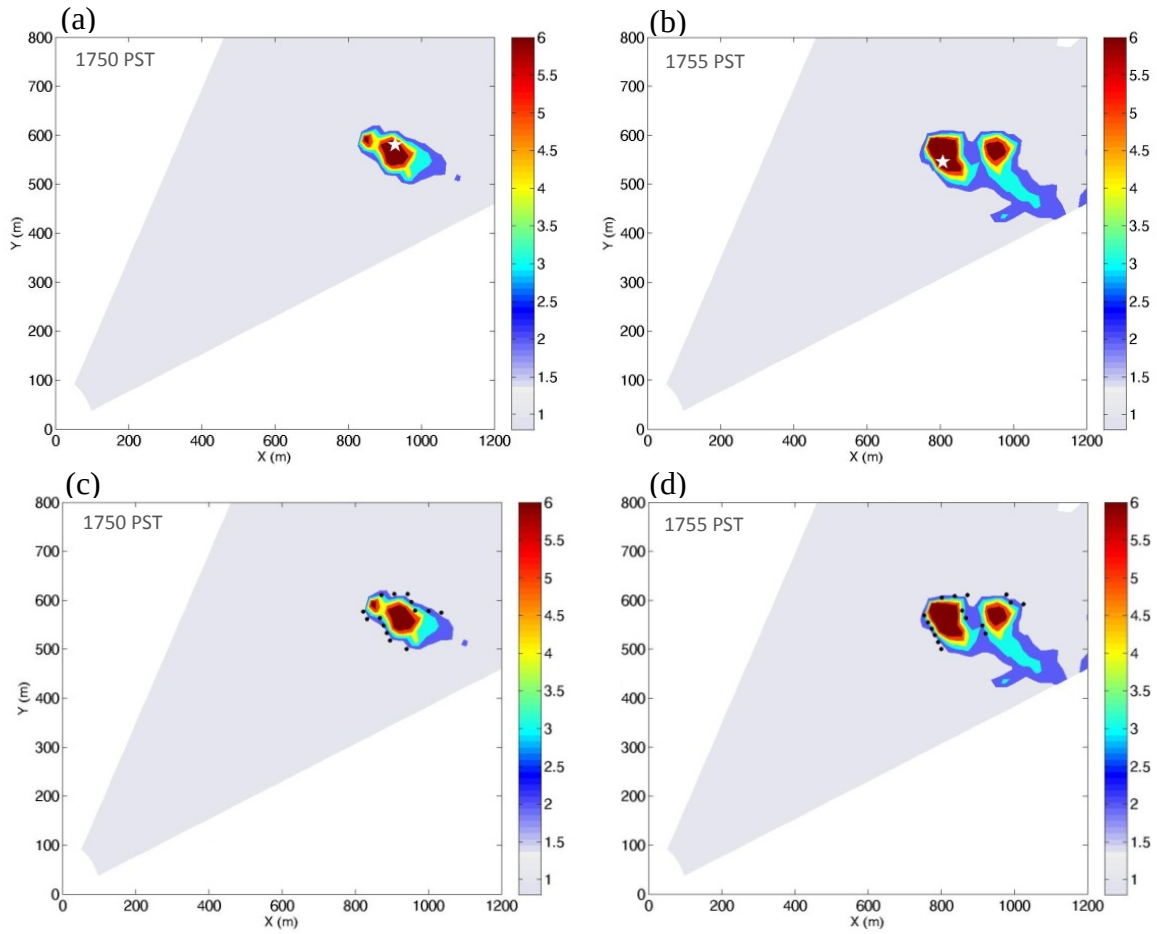

Fig. 23. PPI lidar scans through the plume at specified times. The top images with the white stars show the location of the most intense part of the plume or the convection core. The bottom images show the regions of high backscatter intensity overlaid with the boundaries of the plume (black dots). The tracking of this location works as an indicator of fire spread rate.

5. Conclusions

In this thesis research, preliminary studies tested the capabilities of a scanning Doppler wind lidar. The deployment of the lidar in an urban area allowed for the diurnal study of an urban boundary layer. The lidar also captured the transition of valley winds in a narrow mountain valley from a small experimental study. The kinematic structure of

a wildland fire plume from a low-intensity prescribed burn was also examined with a suite of instruments. Key results from this study included the following:

- Increases in the radial velocities were observed at the plume boundary, indicating acceleration of the wind due to an inflow into the base of the convection column. A rear inflow into the fire front was observed by a reversal of radial velocities behind the plume.
- Convergence zone development was observed downwind of the plume from lidar scans and was confirmed by sodar measurements.
- Fluctuations of the vertical velocity were observed downwind of the fire and indicated turbulence that developed in the plume due to buoyancy produced by the fire. Observations showed an increase in turbulence to 3 $m^2 s^{-2}$ within the fire plume with updraft velocities of 1 m s^{-1}.
- An algorithm was developed to estimate the height of the plume and was used to examine the dispersion of the plume over time. The estimated fire spread rate found from convection core tracking was 0.67 m s^{-1}, while the spread rate of the plume was 2.4 m s^{-1}.

The lidar-scanning techniques that were used can be adjusted in future work to get a better temporal resolution than that obtained during this experiment. With a finer and constant scanning routine, it will also be possible to calculate turbulence statistics from the lidar observations. The prescribed burn was alsoconducted in conditions leading to a

fairly low intensity fire. In the future, the lidar will be mounted in a truck bed allowing for quick deployment on wildland fires during an active fire season.

There are several improvements that can be made to the experimental design in deploying the lidar as discovered during the post-processing procedures outlined in this thesis. One improvement will be in creating faster scanning routines. The atmosphere surrounding a fire is constantly changing and having more scans within shorter time scales will be better for determining the characteristics of the plume. Also, the lidar can only examine the convergence along radial velocity, limiting the analysis to one component of the wind. However, the winds converge into a fire column from all sides. Future studies using dual lidar scanning strategies will examine multiple components of the convergence around the fire and to allow for better analysis of the kinematic structure of a fire plume.

REFERENCES

Banakh, V. A. and C. Werner, 2005: Computer simulation of coherent Doppler lidar measurement of wind velocity and retrieval of turbulent wind statistics. *Opt. Eng*., **44**, 0712051-07120519.

Banta, R. M., L. D. Oliver, E.T. Holloway, R. A. Kropfli, B.W. Bartram, R. E. Cupp, and M.J. Post, 1992: Smoke-column observations from two forest fires using Doppler lidar and Doppler radar. *J. Appl. Meteorol*., **31**, 1328-1349.

Barkwith, A. and C. G. Collier, 2011. Lidar observations of flow variability over complex terrain. *Meteorol. Appl.,* **18**, 372-382.

Bowman, D. M. J. S. et al., 2009: Fire in the earth system. *Science,* **324**, 481-484.

Chen, Z., W. Liu, Y. Ahang, J. He, J. Ruan, S. Li, Y. Cui, 2010: Study on the cloud layer height and properties in Hefei observed by lidar. 5th International Symposium on Advanced Opitcal Manufacturing and Testing Technologies, 6 pp.

Clark, T. L., M. A. Jenkins, J. Coen, and D. Packham, 1996: A coupled atmosphere-fire model: convective feedback on fire-line dynamics. *J. Appl. Meteorol.*, **35**, 875-901.

Clements, C. B., B. E. Potter, and S. Zhong, 2006: In-situ measurements of water vapor, heat, and CO2 fluxes within a prescribed grass fire. *Int. J. Wildland Fire*, **15**(3), 299-306.

---------, S. Zhong, S. Goodrick, J. Li, B. E. Potter, X. Bian, W. E. Heilman, J. J. Charney, R. Perna, M. Jang, D. Lee, M. Patel, S. Street, and G. Aumann, 2007: Observing the dynamics of wildland grass fires. *B. Am. Meteorol. Soc.*, **88**, 1369-1382.

---------, S. Zhong, X. Bian, W. E. Heilman, D. W. Byun, 2008: First observations of turbulence generated by grass fires. *J. Geophys. Res.*, **113**, D22102.

----------, 2010: Thermodynamic structure of a grass fire plume. *Int. J. of Wildland Fire,* **19**, 895-902.

Coen, J., S. Mahalingam, J. Daily, 2004: Infrared imagery of crown-fire dynamics during FROSTFIRE. *J. Appl. Meteoro.*, **43**, 1241-1259.

Cooper, D. I. and W. E. Eichinger, 1994: Structure of the atmosphere in an urban planetary boundary layer from lidar and radiosonde observations. *J. Geophys. Res.*, **99**, 937-948.

Dold, J.W. and A. Zinoviev, 2009: Fire eruption through intensity and spread rate interaction mediated by flow attachment. *Combust. Theor. and Model*., **13**, 763-793.

Frehlich, R., 1996: Effects of wind turbulence on coherent Doppler lidar performance. *J. Atmos. Ocean. Tech.*, **14**, 54-75.

--------- and L. Cornman, 2001: Estimating spatial velocity statistics with coherent Doppler lidar. *J. Atmos. Ocean. Tech.*, **19**, 355-366.

---------, 2008: Doppler Lidar measurements of winds and turbulence in the boundary layer. 14th International Symposium for the Advancement of Boundary Layer Remote Sensing. 11pp.

Kiefer, C. M., C. B. Clements, and B. E. Potter, 2012: Application of a mini Unmanned Aircraft System for in situ monitoring of fire plume thermodynamic properties. *J. Atmos. Ocean. Tech*., **29**, 309-315.

Kiefer, M. T., M. D. Parker, and J. J. Charney, 2009: Regimes of dry convection above wildfires: idealized numerical simulations and dimensional analysis. *J. Atmos. Sci.,* **66**, 806-836.

Kovalev, V. S., J. Newton, C. Wold, and W. M. Hao, 2005: Simple algorithm to determine the near-edge smoke boundaries with scanning lidar. *Appl. Optics*, **44**, 1761-1768.

Krishnamurthy, R., R. Calhoun, B. Billings, and J. Doyle, 2011: Wind turbulence estimates in a valley by coherent Doppler lidar. *Meteorol. Appl*., **18**, 361-371.

Lavoué, D., C. Liousse, H. Cachier, B. J. Stocks, and J. G. Goldammer, 2000: Modeling of carbonaceous particles emitted by boreal and temperate wildfires at northern latitudes. *J. Geophys. Res.,* **105**, 26871-26890.

Linn, R. R., J. L. Winterkamp, C. Edminster, J.J. Colman, and W.S. Smith, 2007: Coupled influences of topography and wind on wildland fire behavior, *Int. J. Wildland Fire*, **16**, 183–195.

Lothon, M., D. H. Lenschow, and S. D. Mayor, 2009: Doppler lidar measurements of vertical velocity spectra in the convective planetary boundary layer. *Bound-Lay. Meteorol.,* **132**, 205-226.

Mandel, J., J. D. Beezley, J. L. Coen, and M. Kim, 2009: Data Assimilation for Wildland Fires: Ensemble Kalman filters in coupled atmosphere-surface models, *IEEE Control Systems Magazine*, **29**, 47–65, doi:10.1109/MCS.2009.932224.

Markowski, P. and Y. Richardson, 2010: Mesoscale meteorology in midlatitudes. Wiley-Blackwell. 407 pp.

Mell, W., M. A. Jenkins, J. Gould, and P. Cheney, 2007: A physics-based approach to modeling grassland fires, *Int. J. Wildland Fire*, **16**, 1–22, doi:10.1071/WF06002.

Menut, L., C. Flamant, J. Pelon, P. H. Flamant, 1999: Urban boundary-layer height determination from measurements over the Paris area. *Appl. Optics*, **38**, 945-954.

Pal, S. R., W. Steinbrecht, A. I. Carswell, 1992: Automated method for lidar determination of cloud-base height and vertical extent. *Appl. Optics*, **31**, 1488-1494.

Pearson, G., F. Davies, and C. Collier, 2009: An analysis of the performance of the UFAM pulsed Doppler lidar for observing the boundary layer. *J. Atmos. Ocean. Tech.*, **26**, 240-250.

---------, F. Davies, and C. Collier, 2010: Remote sensing of the tropical rain forest boundary layer using pulsed Doppler lidar. *J. Atmos. Chem. Phys.*, **10**, 5891-5901.

Potter, B. E., 2005: The role of released moisture in the atmospheric dynamics associated with wildland fires. *Int. J. Wildland Fire*, **14**, 77-84.

Potter, B. E., 2011: Effects of complex terrain on extreme fire behavior, synthesis of knowledge of extreme fire behavior: Volume I for Fire Managers, PNW-GTR-854, USDA.

Rogers, R. R., and W. O. J. Brown, 1997: Radar observations of a major industrial fire. *B. Am. Meteorol. Soc*., **78**, 803-814.

Rotach, M. W., R. Vogt, C. Bernhofer, E. Batchvarova, A. Christen, A. Clappier, B., Feddersen, S.-E. Gryning, G. Martucci, H. Mayer, V. Mitev, T. R. Oke, E., Parlow, H. Richner, M. Roth, Y.-A. Roulet, D. Ruffieux, J.A. Salmod, M. Schatzmann, and J.A. Voogt, 2005: BUBBLE-an urban boundary layer meteorology project. *Theor. Appl. Climatol*. **81**, 231-261.

Rucker, M., R. M. Banta, and D. G. Steyn, 2007: Along-valley structure of daytime thermally driven flows in the Wipp Valley. *J. Appl. Meteorol. Clim.*, **47**, 733-751.

Smalikho, I., 2002: Techniques of wind vector estimation from data measured with a scanning coherent Doppler lidar. *J. Atmos. Ocean. Tech.*, **20**, 276-291.

Sofiev, M., T. Ermakova, and R. Vankevich, 2012: Evaluation of the smoke-injection height from wild-land fires using remote-sensing data. *J. Atmos. Chem. Phys*., **12**, 1995-2006.

Tsai, P., S. J. Fraiser, S. Goodrick, G. Achtemeier, and M. T. Odman, 2009: Combined lidar and radar observations of smoke plumes from prescribed burns: Fourth Symposium on Lidar Atmospheric Applications, 89th Annual Meeting of the American Meteorological Society, 6 pp.

Venema, V., H. Russchenberg, A. Apituley, A. van Lammeren, and L. Ligthart, 2000: Cloud boundary height measurements using lidar and radar. *Phys. Chem. Earth*, **25**, 129-134.

Westerling, A. L., H. G. Hidalgo, D. R. Cayan, T. W. Swetnam, 2006: Warming and earlier spring increase western U.S. forest wildfire activity. *Science*, **313**, 940-943.

Whiteman, C. D., 1982: Breakup of temperature inversions in deep mountain valleys. Part I: Observations. *J. Appl. Meteor*, **21**, 270-289.

---------, 2000: Mountain meteorology: fundamentals and applications. Oxford University Press. 355pp.